Computer Modeling in Engineering & Sciences

Tech Science Press

Doi:10.32604/cmes.2025.065452

ARTICLE

Dynamic Response of a Nonlocal Multiferroic Laminated Composite with Interface Stress Imperfections

Hsin-Yi Kuo* **and Li-Huan Yang**

Department of Civil Engineering, National Yang Ming Chiao Tung University, Hsinchu, 30010, Taiwan

*Corresponding Author: Hsin-Yi Kuo. Email: hykuo@nycu.edu.tw

Received: 13 March 2025; Accepted: 18 June 2025; Published: 31 July 2025

ABSTRACT: This study aims to investigate the propagation of harmonic waves in nonlocal magneto-electro-elastic (MEE) laminated composites with interface stress imperfections using an analytical approach. The pseudo-Stroh formulation and nonlocal theory proposed by Eringen were adopted to derive the propagator matrix for each layer. Both the propagator and interface matrices were formulated to determine the recursive fields. Subsequently, the dispersion equation was obtained by imposing traction-free and magneto-electric circuit open boundary conditions on the top and bottom surfaces of the plate. Dispersion curves, mode shapes, and natural frequencies were calculated for sandwich plates composed of $BaTiO_3$ and $CoFe_2O_4$. Numerical simulations revealed that both interface stress and the nonlocal effect influenced the tuning of the dispersion curve and mode shape for the given layup. The nonlocal effect caused a significant decrease in the dispersion curves, particularly in the high-frequency regions. Additionally, compared to the nonlocal effect, the interface stress exerted a greater influence on the mode shapes. The generalized analytical framework developed in this study provides an effective tool for both the theoretical analysis and practical design of MEE composite laminates.

KEYWORDS: Magneto-electro-elastic; laminated composite; nonlocal; interface stress imperfection; dynamic

1 Introduction

The ongoing trends of device miniaturization has driven significant interest in the magneto-electro-elastic (MEE) nanostructures comprising piezoelectric and piezomagnetic phases. The MEE heterostructures exhibit novel electrical, magnetic, and mechanical properties, offering promising applications in intelligent adaptive systems, including memory devices and energy harvesting [1,2]. Since MEE nanostructures exist at the nanoscale, their behavior and overall properties differ significantly from those of bulk composites. Long-range interatomic and intermolecular cohesive forces play a more significant role in determining the properties of MEE nanostructures [3]. Consequently, size effects must be accounted for in both theoretical and experimental studies [4,5]. While classical continuum mechanics remains a valuable tool, its scale-independent nature may lead to inaccurate results when analyzing nanostructures.

The nonlocal elasticity theory proposed by Eringen [6,7], which accounts for scale effects, offers a computationally efficient alternative to direct atomistic or molecular dynamics simulations [8]. For example, Wu and Li [9] effectively implemented this theory in free vibration analyses of embedded single-layered nanoplates and graphene sheets. Wu and Yu [10] investigated its application to nanobeams and carbon nanotubes (CNT), incorporating nonlocal effects. The application of the theory has been further extended to MEE plates [11–14], and MEE fibrous composites [15–17].

Dynamic responses of MEE composites, such as wave propagation and free vibration, have attracted significant research attention in recent years. Fundamental to the design process is determining natural frequencies and corresponding vibration modes-an analysis that has become a focal point in several studies. For example, Liu et al. [18] developed a dynamic analysis method for three-phase MEE structures using overlapping triangular finite elements. Jiang et al. [19] created a coupled MEE edge-based smoothed finite element method to evaluate the dynamic behavior of MEE solids. Kuo et al. [20] systematically compared wave propagation characteristics in MEE laminated composites with varying layering directions. Ly et al. [21] introduced a numerical approach for nonlinear analysis and smart damping control in functionally graded CNT reinforced MEE plate.

Most studies assume perfectly bonded interfaces between different phases-an idealized condition that may not reflect real-world scenarios. However, interfaces often exhibit imperfections due to cracking, dislocations, aging, or manufacturing defects. Additionally, these interfacial imperfections significantly affect magneto-electric coupling effects. Several studies have addressed interfacial imperfections in MEE composites, including [22–24] for static cases and [25,26] for dynamic cases.

Therefore, this study aims to investigate MEE laminates using the nonlocal theory proposed by Eringen, with a particular focus on extended interface stress-type contact condition. The paper is organized as follows. Section 2 presents the formulation of the multifield boundary-value problem, including considerations of extended interface stress imperfections. Section 3 presents the derivation of the field solutions for each homogeneous layer using the pseudo-Stroh formulation. A recursive framework that incorporates both propagation and interface matrices is developed to account for imperfect interface characteristics and determine exact solutions throughout the laminate. Section 4 discusses particular numerical cases analyzing the effect of the interface stress and nonlocal length parameters. Section 5 provides conclusions remarks.

2 Basic Formulations

2.1 Nonlocal Theory for MEE Materials

We consider a three-dimensional N–bonded orthotropic and rectangular MEE plate with nonlocal effect as shown in Fig. 1. A global Cartesian coordinate system (x, y, z) is attached to the laminate such that the bottom surfaces of the plate is set as the horizontal coordinate plane $x - z$. The plate is horizontally infinite but vertically finite in the y–direction with the total thickness H. The lower and upper interfaces of the jth layer are defined as y_{j-1}^{+} and y_{j}^{-}, respectively, with the thickness $h_j = y_j^{-} - y_{j-1}^{+}$. The internal interfaces between the adjacent plates are imperfectly connected, which will be discussed later on. The fabrication of the type of MEE laminated composites can be referred to the work by Dong et al. [27], Wang et al. [28], and Zhai et al. [29].

Following Pan and Waksmanski [13], the constitutive relations of a nonlocal linear anisotropic MEE within the context of nonlocal model proposed by Eringen can be expressed as

$$\begin{aligned}
&\sigma_{ij}^{g} - l^2\nabla^2\sigma_{ij}^{g} = \sigma_{ij}^{c} = c_{ijkl}\varepsilon_{kl} - e_{kij}E_k - q_{kij}H_k,\\
&D_{i}^{g} - l^2\nabla^2 D_{i}^{g} = D_{i}^{c} = e_{ijk}\varepsilon_{jk} + \kappa_{ij}E_j + \lambda_{ji}H_j,\\
&B_{i}^{g} - l^2\nabla^2 B_{i}^{g} = B_{i}^{c} = q_{ijk}\varepsilon_{jk} + \lambda_{ij}E_j + \mu_{ij}H_j,
\end{aligned} \tag{1}$$

where ∇^2 is the 3D Laplace operator; l is the nonlocal length parameter. σ_{ij}, ε_{ij}, D_i, E_i, B_i and H_i are the stress, strain, electric displacement, electric field, magnetic flux density, and magnetic field. c_{ijkl}, e_{ijk}, q_{ijk}, κ_{ij}, μ_{ij}, and λ_{ij} are elastic stiffness constant, piezoelectric coefficient, piezomagnetic coefficient, dielectric permittivity, magnetic permeability, and magnetoelectric coupling coefficient. The upper index g denotes the nonlocal field quantities, while the upper index c denotes the classical field quantities.

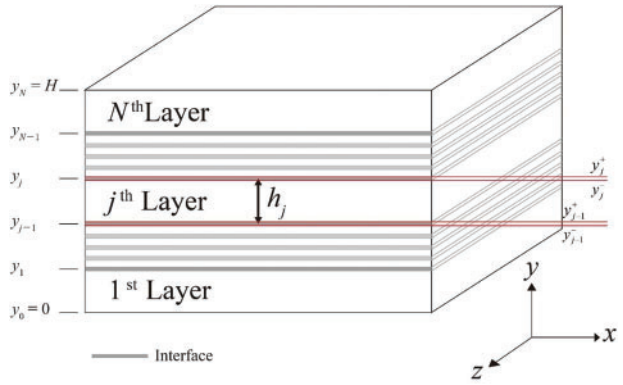

Figure 1: Geometry and coordinate system of an N-bonded orthotropic, nonlocal rectangular linearly MEE plate. The laminated plate is horizontally infinite but vertically finite in the y-direction with total thickness H. The jth layer is bonded by its lower interface y_{j-1^+} and upper interface y_{j^-}. The interfaces between the plates are imperfectly connected

The infinitesimal strain ε_{ij}, electric field E_i, and magnetic field H_i can be derived from the gradient of the elastic displacement u_i, electric potential ϕ, and magnetic potential ψ as follows:

$$\varepsilon_{ij} = \frac{1}{2}\left(u_{i,j} + u_{j,i}\right),\ E_i = -\phi_{,i},\ H_i = -\psi_{,i}, \tag{2}$$

for which comma followed by lowercase subscript i denotes partial derivative.

For each individual plate, the equilibrium equations for the stress, electric displacement, and magnetic flux in the absence of body forces and electric sources are defined by

$$\sigma^g_{ij,j} = \rho\frac{\partial^2 u_i}{\partial t^2},\ D^g_{i,i} = 0,\ B^g_{i,i} = 0. \tag{3}$$

Here ρ is the mass density and t is time.

3 Free Vibration Analysis of the MEE Laminate

3.1 Field Solutions for Each Nonlocal Plate

We consider the material is orthotropic symmetry. The polarization and magnetization directions are along the $z-$axis. The involved material coefficients with the three orthogonal planes of symmetry along the $x-$, $y-$, $z-$directions can be expressed in the matrix form as

$$\mathbf{C} = \begin{bmatrix} C_{11} & C_{12} & C_{13} & 0 & 0 & 0 \\ & C_{22} & C_{23} & 0 & 0 & 0 \\ & & C_{33} & 0 & 0 & 0 \\ & & & C_{44} & 0 & 0 \\ & symm & & & C_{55} & 0 \\ & & & & & C_{66} \end{bmatrix},$$

$$\mathbf{e}^T = \begin{bmatrix} 0 & 0 & e_{31} \\ 0 & 0 & e_{32} \\ 0 & 0 & e_{33} \\ 0 & e_{24} & 0 \\ e_{15} & 0 & 0 \\ 0 & 0 & 0 \end{bmatrix}, \ \mathbf{q}^T = \begin{bmatrix} 0 & 0 & q_{31} \\ 0 & 0 & q_{32} \\ 0 & 0 & q_{33} \\ 0 & q_{24} & 0 \\ q_{15} & 0 & 0 \\ 0 & 0 & 0 \end{bmatrix},$$

$$\boldsymbol{\kappa} = \begin{bmatrix} \kappa_{11} & 0 & 0 \\ 0 & \kappa_{22} & 0 \\ 0 & 0 & \kappa_{33} \end{bmatrix}, \ \boldsymbol{\mu} = \begin{bmatrix} \mu_{11} & 0 & 0 \\ 0 & \mu_{22} & 0 \\ 0 & 0 & \mu_{33} \end{bmatrix}, \ \boldsymbol{\lambda} = \begin{bmatrix} \lambda_{11} & 0 & 0 \\ 0 & \lambda_{22} & 0 \\ 0 & 0 & \lambda_{33} \end{bmatrix}. \tag{4}$$

Here C_{IJ}, e_{iJ}, and q_{iJ} $(i = 1-3,\ I, J = 1-6)$ are elastic stiffness constant, piezoelectric coefficient and piezomagnetic coefficient in the Voigt notation.

Assuming time-harmonic vibration motion, the field solutions are sought in the form of

$$\boldsymbol{\Phi} = \begin{pmatrix} u_1 \\ u_2 \\ u_3 \\ \phi \\ \psi \end{pmatrix} = \sum_{m,\,n} e^{i(k_1 x + k_2 y + k_3 z - \omega t)} \mathbf{a}, \ \mathbf{a} = \begin{pmatrix} a_1 \\ a_2 \\ a_3 \\ a_4 \\ a_5 \end{pmatrix},$$

$$\boldsymbol{\Sigma}_n^g = \begin{pmatrix} \sigma_{21}^g \\ \sigma_{22}^g \\ \sigma_{23}^g \\ D_2^g \\ B_2^g \end{pmatrix} = \sum_{m,\,n} e^{i(k_1 x + k_2 y + k_3 z - \omega t)} \mathbf{b}, \ \mathbf{b} = \begin{pmatrix} b_1 \\ b_2 \\ b_3 \\ b_4 \\ b_5 \end{pmatrix},$$

$$\boldsymbol{\Sigma}_n^c = \begin{pmatrix} \sigma_{21}^c \\ \sigma_{22}^c \\ \sigma_{23}^c \\ D_2^c \\ B_2^c \end{pmatrix} = \sum_{m,\,n} e^{i(k_1 x + k_2 y + k_3 z - \omega t)} \mathbf{d}, \ \mathbf{d} = \begin{pmatrix} d_1 \\ d_2 \\ d_3 \\ d_4 \\ d_5 \end{pmatrix}, \tag{5}$$

where ω is the angular vibration frequency of the excitation, and $i = \sqrt{-1}$. k_1, k_3 are the components of the wave vector depending on the angle of the wavenumber along the propagating direction in the $x - z$ plane. k_2 is an unknown to be determined. **a, b, d** are unknown amplitudes to be determined.

Substituting Eqs. (4) and (5) into Eqs. (1) and (2), the nonlocal constitutive relation yields

$$\left[1 + l^2\left(k_1^2 + k_2^2 + k_3^2\right)\right]\mathbf{b} = i\left(\mathbf{R}^T + k_2\mathbf{T}\right)\mathbf{a}, \tag{6}$$

where matrices **R** and **T** are given by

$$\mathbf{R} = \begin{bmatrix} 0 & C_{12}k_1 & 0 & 0 & 0 \\ C_{66}k_1 & 0 & C_{44}k_3 & e_{24}k_3 & q_{24}k_3 \\ 0 & C_{23}k_3 & 0 & 0 & 0 \\ 0 & e_{32}k_3 & 0 & 0 & 0 \\ 0 & q_{32}k_3 & 0 & 0 & 0 \end{bmatrix}, \ \mathbf{T} = \begin{bmatrix} C_{66} & 0 & 0 & 0 & 0 \\ & C_{22} & 0 & 0 & 0 \\ & & C_{44} & e_{24} & q_{24} \\ & symm & & -\kappa_{22} & -\lambda_{22} \\ & & & & -\mu_{22} \end{bmatrix}. \tag{7}$$

Furthermore, inserting Eq. (5) into the governing Eq. (3) leads to a quadratic eigenequation, as follows:

$$\left[\mathbf{Q}_n + k_2\left(\mathbf{R}+\mathbf{R}^T\right) + k_2^2\mathbf{T}_n\right]\mathbf{a} = \mathbf{0}. \tag{8}$$

Finally, the above equation with the help of Eq. (6) can further be converted into the linear eigensystem of equations

$$\begin{bmatrix} -\mathbf{T}_n^{-1}\mathbf{R}^T & -i\mathbf{T}_n^{-1} \\ -i\left(\mathbf{Q}_n - \mathbf{R}\mathbf{T}_n^{-1}\mathbf{R}^T\right) & -\mathbf{R}\mathbf{T}_n^{-1} \end{bmatrix}\begin{bmatrix} \mathbf{a} \\ \mathbf{d} \end{bmatrix} = k_2\begin{bmatrix} \mathbf{a} \\ \mathbf{d} \end{bmatrix}. \tag{9}$$

Here

$$\mathbf{Q}_n \equiv \mathbf{Q} - \left[1 + l^2\left(k_1^2 + k_3^2\right)\right]\rho\omega^2\mathbf{I}_3,\ \mathbf{T}_n \equiv \mathbf{T} - \rho\omega^2 l^2\mathbf{I}_3,$$

$$\mathbf{Q} = \begin{bmatrix} C_{11}k_1^2 + C_{55}k_3^2 & 0 & k_1k_3\left(C_{13}+C_{55}\right) & k_1k_3\left(e_{15}+e_{31}\right) & k_1k_3\left(q_{15}+q_{31}\right) \\ & C_{66}k_1^2 + C_{44}k_3^2 & 0 & 0 & 0 \\ & & C_{55}k_1^2 + C_{33}k_3^2 & e_{15}k_1^2 + e_{33}k_3^2 & q_{15}k_1^2 + q_{33}k_3^2 \\ & symm & & -\left(\kappa_{11}k_1^2 + \kappa_{33}k_3^2\right) & -\left(d_{11}k_1^2 + d_{33}k_3^2\right) \\ & & & & -\left(\mu_{11}k_1^2 + \mu_{33}k_3^2\right) \end{bmatrix},$$

$\mathbf{I}_3$ is a 3×3 unit matrix, and the 5×1 constant column matrix $\mathbf{d}$ is related to $\mathbf{a}$ by

$$\mathbf{d} = i\left(\mathbf{R}^T + k_2\mathbf{T}\right)\mathbf{a}, \tag{10}$$

from the constitutive law (1).

Without the proportional position term $e^{e^{i(k_1x+k_3z)}}$ and the time-dependent factor $e^{i\omega t}$ in (5) for clarity, the general $y-$ dependent solution for the extended displacement and traction expansion coefficient vectors can be expressed as

$$\begin{bmatrix} \widetilde{\mathbf{\Phi}}(y) \\ \widetilde{\mathbf{\Sigma}}_n^g(y) \end{bmatrix} = \begin{bmatrix} \mathbf{A}_{\text{I}} & \mathbf{A}_{\text{II}} \\ \mathbf{B}_{\text{I}} & \mathbf{B}_{\text{II}} \end{bmatrix}\left\langle e^{i\mathbf{k}y}\right\rangle\begin{bmatrix} \mathbf{K}_{\text{I}} \\ \mathbf{K}_{\text{II}} \end{bmatrix}, \tag{11}$$

with

$$\widetilde{\mathbf{\Phi}}(y) = e^{ik_2y}\mathbf{a},\ \widetilde{\mathbf{\Sigma}}_n(y) = e^{ik_2y}\mathbf{b}, \tag{12}$$

$$\left\langle e^{i\mathbf{k}y}\right\rangle = diag\left(e^{ik_2^{(1)}y}, e^{ik_2^{(2)}y}, e^{ik_2^{(3)}y}, e^{ik_2^{(4)}y}, e^{ik_2^{(5)}y}, e^{ik_2^{(6)}y}, e^{ik_2^{(7)}y}, e^{ik_2^{(8)}y}, e^{ik_2^{(9)}y}, e^{ik_2^{(10)}y}\right),$$

and $\mathbf{A}_{\text{I}}, \mathbf{A}_{\text{II}}, \mathbf{B}_{\text{I}}, \mathbf{B}_{\text{II}}$ being the eigenvector matrices defined by

$$\mathbf{A}_{\text{I}} = \left(\ \mathbf{a}_1,\ \mathbf{a}_2,\ \mathbf{a}_3,\ \mathbf{a}_4,\ \mathbf{a}_5\ \right),\ \mathbf{A}_{\text{II}} = \left(\ \mathbf{a}_6,\ \mathbf{a}_7,\ \mathbf{a}_8,\ \mathbf{a}_9,\ \mathbf{a}_{10}\ \right),$$
$$\mathbf{B}_{\text{I}} = \left(\ \mathbf{b}_1,\ \mathbf{b}_2,\ \mathbf{b}_3,\ \mathbf{b}_4,\ \mathbf{b}_5\ \right),\ \mathbf{B}_{\text{II}} = \left(\ \mathbf{b}_6,\ \mathbf{b}_7,\ \mathbf{b}_8,\ \mathbf{b}_9,\ \mathbf{b}_{10}\ \right),$$

here $\mathbf{K}_{\text{I}}$ and $\mathbf{K}_{\text{II}}$ are two 5×1 constant column matrices to be determined from the internal and external boundary conditions of the plate; k_2 and $\{\mathbf{a}_i, \mathbf{d}_i\}$ are the eigenvalue and corresponding eigenvectors of Eq. (9), and $\mathbf{b}_i$ can be calculated from (6).

By eliminating the involved undetermined coefficients constants $\mathbf{K}_1$ and $\mathbf{K}_2$ in Eq. (11), the extended displacement and traction on the top and bottom of the jth layer can be related as

$$\begin{bmatrix} \widetilde{\mathbf{\Phi}}\left(y_j^-\right) \\ \widetilde{\mathbf{\Sigma}}_n^g\left(y_j^-\right) \end{bmatrix} = \mathbf{P}_j\left(h_j\right)\begin{bmatrix} \widetilde{\mathbf{\Phi}}\left(y_{j-1}^+\right) \\ \widetilde{\mathbf{\Sigma}}_n^g\left(y_{j-1}^+\right) \end{bmatrix}, \tag{13}$$

where

$$\mathbf{P}_j\left(y\right) = \begin{bmatrix} \mathbf{A}_1 & \mathbf{A}_2 \\ \mathbf{B}_1 & \mathbf{B}_2 \end{bmatrix}\left\langle e^{i\mathbf{k}\left(y-y_j\right)}\right\rangle\begin{bmatrix} \mathbf{A}_1 & \mathbf{A}_2 \\ \mathbf{B}_1 & \mathbf{B}_2 \end{bmatrix}^{-1}, \tag{14}$$

is the propagation matrix of the jth layer.

In order to complete the total field solutions, the remaining in-plane stress, electric displacement, and magnetic flux density are organized as follows:

$$\mathbf{\Sigma}_t^g = \begin{bmatrix} \sigma_{11} \\ \sigma_{33} \\ \sigma_{13} \\ D_1 \\ D_3 \\ B_1 \\ B_3 \end{bmatrix} = \sum_{m,\,n} e^{i\left(k_1 x + k_2 y + k_3 z - \omega t\right)}\mathbf{c},\ \mathbf{c}=\begin{pmatrix} c_1 \\ c_2 \\ c_3 \\ c_4 \\ c_5 \\ c_6 \\ c_7 \end{pmatrix}. \tag{15}$$

Substituting the extended displacement expansion in Eq. (5) and Eq. (15) into the constitutive relation (1), additional relations between the associated expansion coefficients are derived as

$$\left[1 + l^2\left(k_1^2 + k_2^2 + k_3^2\right)\right]\mathbf{c} = i\begin{bmatrix} C_{11}k_1 & C_{12}k_2 & C_{13}k_3 & e_{31}k_3 & q_{31}k_3 \\ C_{13}k_1 & C_{23}k_2 & C_{33}k_3 & e_{33}k_3 & q_{33}k_3 \\ C_{55}k_3 & 0 & C_{55}k_1 & e_{15}k_1 & q_{15}k_1 \\ e_{15}k_3 & 0 & e_{15}k_1 & -\kappa_{11}k_1 & -\lambda_{11}k_1 \\ e_{31}k_1 & e_{32}k_2 & e_{33}k_3 & -\kappa_{33}k_3 & -\lambda_{33}k_3 \\ q_{15}k_3 & 0 & q_{15}k_1 & -\lambda_{11}k_1 & -\mu_{11}k_1 \\ q_{31}k_1 & q_{32}k_2 & q_{33}k_3 & -\lambda_{33}k_3 & -\mu_{33}k_3 \end{bmatrix}\mathbf{a}. \tag{16}$$

3.2 Interface Stress-Type Imperfect Interface

To find the exact solutions, we need the interfacial conditions. We consider the extended interface stress interfacial conditions [30]:

$$\begin{aligned} &\left[\left[\mathbf{\Phi}\right]\right]_{y_j} = \mathbf{0},\ \left[\left[\sigma_{2\alpha}^c\right]\right] = -f_{\alpha\beta\gamma\mu}u_{\gamma,\mu\beta}, \\ &\left[\left[\sigma_{22}^c\right]\right] = 0,\ \left[\left[D_2^c\right]\right] = \kappa_{\alpha\beta}^f\phi_{,\alpha\beta},\ \left[\left[B_2^c\right]\right] = \mu_{\alpha\beta}^f\psi_{,\alpha\beta}, \end{aligned}\quad \alpha,\beta,\gamma,\mu = 1,3, \tag{17}$$

where $\left[\left[\cdot\right]\right]$ denotes that the corresponding physical quantity has a jump across the interface. $f_{\alpha\beta\gamma\mu}$, $\kappa_{\alpha\beta}^f$, $\mu_{\alpha\beta}^f$ denote the interface elastic modulus, interface electric permittivity, and interface magnetic permeability, respectively. Next, we rearrange the above extended interface stress-type interfacial condition as

$$\begin{bmatrix} \widetilde{\mathbf{\Phi}}\left(y_{j^+}\right) \\ \widetilde{\mathbf{\Sigma}}_n^c\left(y_{j^+}\right) \end{bmatrix} = \mathbf{M}_j\begin{bmatrix} \widetilde{\mathbf{\Phi}}\left(y_{j^-}\right) \\ \widetilde{\mathbf{\Sigma}}_n^c\left(y_{j^-}\right) \end{bmatrix}, \tag{18}$$

where the interface matrix $\mathbf{M}_j$ at the interface $y = y_j$ is defined as

$$\mathbf{M}_j = \begin{bmatrix} \mathbf{I}_5 & \mathbf{0} \\ \mathbf{L}_j & \mathbf{I}_5 \end{bmatrix}. \tag{19}$$

Here $\mathbf{I}_5$ is a 5×5 unit matrix and

$$\mathbf{L}_j = \begin{bmatrix} k_1^2 f_{1111} + k_3^2 f_{1313} & 0 & k_1 k_3 \left(f_{1133} + f_{1313}\right) & 0 & 0 \\ & 0 & 0 & 0 & 0 \\ & & k_1^2 f_{1313} + k_3^2 f_{3333} & 0 & 0 \\ & symm & & -k_1^2 \kappa_{11}^f - k_3^2 \kappa_{33}^f & 0 \\ & & & & -k_1^2 \mu_{11}^f - k_3^2 \mu_{33}^f \end{bmatrix}. \tag{20}$$

3.3 Recursive Field Solutions in the Laminate

Transferring the general field solution from the jth layer to the next $j+1$th layer with an imperfect interface y_j in between, we need to combine Eqs. (13) and (18). However, the former is related to the nonlocal extended traction while the latter is related to the classical extended traction. To connect the nonlocal and classical extended traction fields, we notice that

$$\begin{bmatrix} \widetilde{\mathbf{\Phi}}(y) \\ \widetilde{\mathbf{\Sigma}}_n^c(y) \end{bmatrix} = \begin{bmatrix} \mathbf{A}_{\mathrm{I}} & \mathbf{A}_{\mathrm{II}} \\ \mathbf{D}_{\mathrm{I}} & \mathbf{D}_{\mathrm{II}} \end{bmatrix} \left\langle e^{i\mathbf{k}y} \right\rangle \begin{bmatrix} \mathbf{K}_{\mathrm{I}} \\ \mathbf{K}_{\mathrm{II}} \end{bmatrix}, \tag{21}$$

where

$$\mathbf{D}_{\mathrm{I}} = \begin{pmatrix} \mathbf{d}_1, & \mathbf{d}_2, & \mathbf{d}_3, & \mathbf{d}_4, & \mathbf{d}_5 \end{pmatrix}, \mathbf{D}_{\mathrm{II}} = \begin{pmatrix} \mathbf{d}_6, & \mathbf{d}_7, & \mathbf{d}_8, & \mathbf{d}_9, & \mathbf{d}_{10} \end{pmatrix}.$$

Combining (11) and (21) and then substituting the result into (18) yields

$$\begin{bmatrix} \widetilde{\mathbf{\Phi}}\left(y_{j+}\right) \\ \widetilde{\mathbf{\Sigma}}_n^g\left(y_{j+}\right) \end{bmatrix} = \mathbf{M}_j^g \begin{bmatrix} \widetilde{\mathbf{\Phi}}\left(y_{j-}\right) \\ \widetilde{\mathbf{\Sigma}}_n^g\left(y_{j-}\right) \end{bmatrix}, \tag{22}$$

where

$$\mathbf{M}_j^g = \begin{bmatrix} \mathbf{A}_{\mathrm{I}} & \mathbf{A}_{\mathrm{II}} \\ \mathbf{B}_{\mathrm{I}} & \mathbf{B}_{\mathrm{II}} \end{bmatrix} \begin{bmatrix} \mathbf{A}_{\mathrm{I}} & \mathbf{A}_{\mathrm{II}} \\ \mathbf{D}_{\mathrm{I}} & \mathbf{D}_{\mathrm{II}} \end{bmatrix}^{-1} \mathbf{M}_j \begin{bmatrix} \mathbf{A}_{\mathrm{I}} & \mathbf{A}_{\mathrm{II}} \\ \mathbf{D}_{\mathrm{I}} & \mathbf{D}_{\mathrm{II}} \end{bmatrix} \begin{bmatrix} \mathbf{A}_{\mathrm{I}} & \mathbf{A}_{\mathrm{II}} \\ \mathbf{B}_{\mathrm{I}} & \mathbf{B}_{\mathrm{II}} \end{bmatrix}^{-1}.$$

Therefore, when transferring the solution from the jth layer to the next $j+1$th layer with an imperfect interface y_j in between, we only need to multiply the interface matrix between the two layer matrices $\mathbf{P}_j(h_j)$ and $\mathbf{P}_{j+1}(h_{j+1})$ to obtain

$$\begin{bmatrix} \widetilde{\mathbf{\Phi}}\left(y_{j+1^-}\right) \\ \widetilde{\mathbf{\Sigma}}_n^g\left(y_{j+1^-}\right) \end{bmatrix} = \mathbf{P}_{j+1}\left(h_{j+1}\right) \mathbf{M}_j^g \mathbf{P}_j\left(h_j\right) \begin{bmatrix} \widetilde{\mathbf{\Phi}}\left(y_{j-1^+}\right) \\ \widetilde{\mathbf{\Sigma}}_n^g\left(y_{j-1^+}\right) \end{bmatrix}. \tag{23}$$

Here the propagator matrix $\mathbf{P}_j(y)$ is defined in Eq. (14). A similar recursive relation for the field quantities as Eq. (23) from the bottom surface to any field point y in the kth layer ($y_{k-1} \le y \le y_k$) can be expressed as follows:

$$\begin{bmatrix} \widetilde{\mathbf{\Phi}}(y) \\ \widetilde{\mathbf{\Sigma}}_n^g(y) \end{bmatrix} = \mathbf{P}_k\left(y - y_{k-1}\right) \mathbf{M}_{k-1} \mathbf{P}_{k-1}\left(h_{k-1}\right) \cdots \mathbf{P}_2\left(h_2\right) \mathbf{M}_1 \mathbf{P}_1\left(h_1\right) \begin{bmatrix} \widetilde{\mathbf{\Phi}}(0) \\ \widetilde{\mathbf{\Sigma}}_n^g(0) \end{bmatrix}. \tag{24}$$

The prescribed boundary conditions on both bottom $y = 0$ and top $y = H$ surfaces are traction free and magneto-electric circuit open. That is

$$\widetilde{\mathbf{\Sigma}}_n^g(0) = \widetilde{\mathbf{\Sigma}}_n^g(H) = \mathbf{0}. \tag{25}$$

By means of the above boundary conditions, the recursive field

$$\begin{bmatrix} \widetilde{\mathbf{\Phi}}(H) \\ \widetilde{\mathbf{\Sigma}}_n^g(H) \end{bmatrix} = \begin{bmatrix} \mathbf{S}_{11} & \mathbf{S}_{12} \\ \mathbf{S}_{21} & \mathbf{S}_{22} \end{bmatrix} \begin{bmatrix} \widetilde{\mathbf{\Phi}}(0) \\ \widetilde{\mathbf{\Sigma}}_n^g(0) \end{bmatrix} \tag{26}$$

$$\begin{bmatrix} \mathbf{S}_{11} & \mathbf{S}_{12} \\ \mathbf{S}_{21} & \mathbf{S}_{22} \end{bmatrix} = \mathbf{P}_N(h_N)\,\mathbf{M}_{N-1}^g \cdots \mathbf{M}_2^g \mathbf{P}_2(h_2)\,\mathbf{M}_1^g \mathbf{P}_1(h_1),$$

yields the dispersion equation

$$\det \mathbf{S}_{21} = 0. \tag{27}$$

4 Numerical Results and Discussion

To investigate the behavior of nonlocal effects and interface stresses, the proposed solution was applied to a sandwich plate composed of piezoelectric barium titanate ($BaTiO_3$, BTO) and piezomagnetic cobalt ferrite ($CoFe_2O_4$, CFO). Two laminate configurations were examined: (1) a BTO/CFO/BTO layered structure and (2) a CFO/BTO/CFO layered structure. All three layers were assumed to have equal thickness, while the materials were transversely isotropic. The material properties used in the numerical analysis were as follows: $C_{11} = 166GPa$, $C_{12} = 77GPa$, $C_{13} = 78GPa$, $C_{33} = 162GPa$, $C_{44} = 43GPa$, $e_{15} = 11.6C/m^2$, $e_{31} = -4.4C/m^2$, $e_{33} = 18.6C/m^2$, $\kappa_{11} = 11.2nC^2/Nm^2$, $\kappa_{33} = 12.6nC^2/Nm^2$, $\mu_{11} = 5\mu Ns^2/C^2$, $\mu_{33} = 10\mu Ns^2/C^2$, $\rho = 5800kg/m^3$ for BTO, and $C_{11} = 286GPa$, $C_{12} = 173GPa$, $C_{13} = 170.5GPa$, $C_{33} = 269.5GPa$, $C_{44} = 45.3GPa$, $q_{15} = 550N/Am$, $q_{31} = 580.3N/Am$, $q_{33} = 699.7N/Am$, $\kappa_{11} = 0.08nC^2/Nm^2$, $\kappa_{33} = 0.093nC^2/Nm^2$, $\mu_{11} = 590\mu Ns^2/C^2$, $\mu_{33} = 157\mu Ns^2/C^2$, $\rho = 5300kg/m^3$ for CFO [31].

The imperfect interface was modeled as a thin interphase layer c with thickness δ and distinct material properties. The interphase properties were characterized by [30]

$$f_{1111} = f_{3333} = \lambda_f + 2G_f,\ f_{1133} = \lambda_f,\ f_{1313} = G_f,\ \kappa_{\alpha\beta}^f = \kappa_f,\ \mu_{\alpha\beta}^f = \mu_f. \tag{28}$$

where

$$\lambda_f = \frac{2G_c\lambda_c\delta}{\lambda_c + 2G_c}, G_f = \delta G_c,\ \kappa_f = \delta\kappa_c,\ \mu_f = \delta\mu_c,$$

here λ_c represents the Lamé constant, G_c indicates the shear modulus, κ_c is the dielectric permittivity, and μ_c represents the magnetic permeability. For the analysis, the following assumptions were made

$$C_c = \Gamma_m C_{\max}/\delta,\ G_c = \Gamma_m G_{\max}/\delta,\ \kappa_c = \Gamma_m \kappa_{\max}/\delta,\ \mu_c = \Gamma_m \mu_{\max}/\delta, \tag{29}$$

where Γ_m represents the relative scaling parameter, and $C_{\max}$, $G_{\max}$, $\kappa_{\max}$, and $\mu_{\max}$ denote the maximum values of the elastic constant, dielectric permittivity, and magnetic permeability from the BTO and CFO constituents, respectively. Different interface conditions were investigated: perfect contact, $\Gamma_m = 10^{-1}$ and $\Gamma_m = 10^0$. The perfect contact condition maintained continuity in both extended displacement and traction vectors across the interface. The relative scaling parameter Γ_m directly correlated with interfacial

stiffness and electromagnetic properties-higher values indicated stiffer interfaces with stronger dielectric constant and magnetic permeability. We analyzed three different nonlocal length-to-thickness ratios (l/H = 0,0.06, 0.12). For modeling simplicity, identical nonlocal lengths were maintained across all material layers in each analysis case.

For numerical analysis, the wave was assumed to propagate exclusively along the $x-$axis ($k = k_1,\ k_3 = 0$). The wave was decoupled into a Lamb wave ($u_3 = 0$) and a Love wave ($u_1 = 0$ and $u_2 = 0$). Dimensionless frequency $\Omega = \omega H\sqrt{\rho_{\max}/C_{\max}}$ and dimensionless wavenumber kH were used, where $C_{\max}$ and $\rho_{\max}$ represent the maximum elastic modulus and density of the constituents, respectively. An efficient root-finding algorithm developed by Zhu et al. [32] was employed to obtain the accurate solutions.

4.1 Lamb Wave

Figs. 2 and 3 illustrate the dispersion curves for the first three Lamb wave modes of nonlocal BTO/CFO/BTO and CFO/BTO/CFO sandwich plates. The results showed that the dispersion curves for the classical case (i.e., $l/H = 0$) of the BTO/CFO/BTO configuration are consistent with those of a previous study [26]. Furthermore, significant influence of the nonlocal effect was observed. The dispersion curves associated with the same branches differed significantly between the classical and nonlocal modes. Specifically, the inclusion of the nonlocal length reduced the dispersion curve values, particularly in the high-frequency regimes (i.e., at high wavenumbers and short wavelengths). Additionally, the nonlocal effect altered the overall trends of the dispersion behavior; as the nonlocal length increased, the curves exhibited faster convergence. The slope of the dispersion curves in the nonlocal plate decreased as the wavenumber increased. The nonlocal length indicated the spatial range over which a material point could exert an instantaneous effect. As the nonlocal length increased-indicating a broader interaction domain [6,7]-the slope of the dispersion curves decreased further in high-frequency regions. These findings demonstrate that nonlocal effects become critically significant for high-frequency device operation.

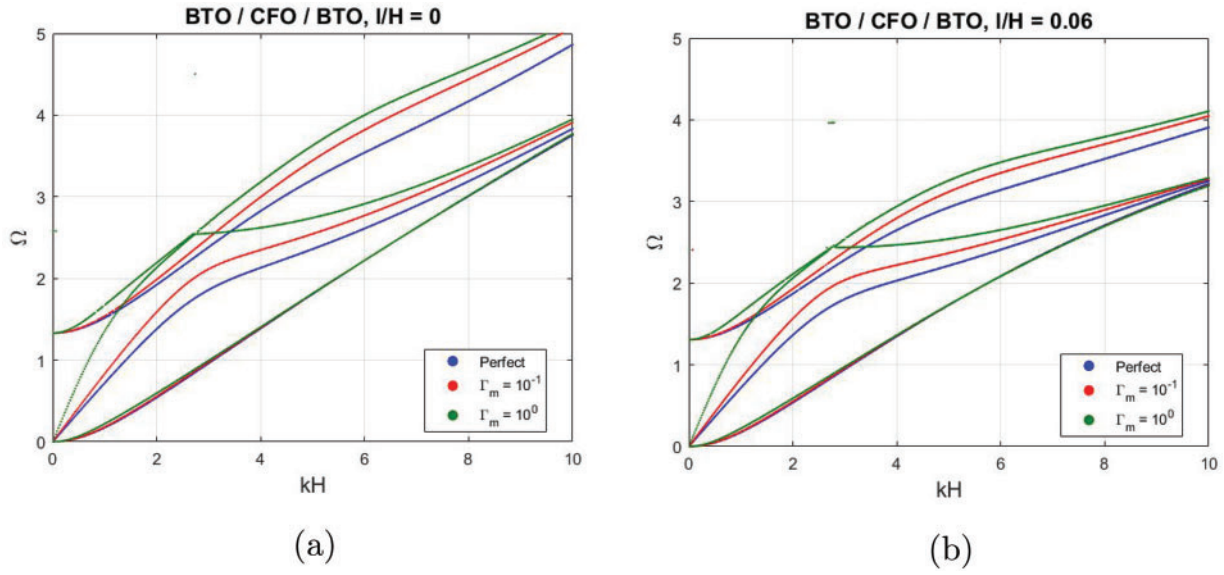

Figure 2: (Continued)

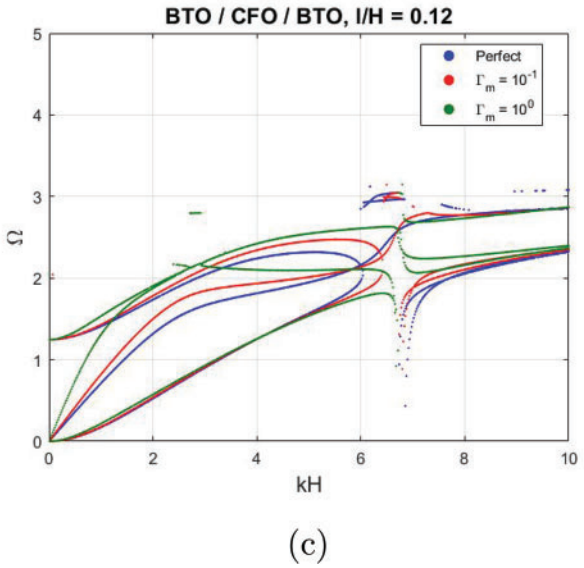

Figure 2: Dispersion curves for Lamb waves in a BTO/CFO/BTO sandwich plate with different interface contacts: perfect contact, imperfect contact with the relative scaling parameter $\Gamma_m = 10^{-1}$, $\Gamma_m = 10^0$. Dimensionless nonlocal length parameter **(a)** $l/H = 0$, **(c)** $l/H = 0.06$, **(c)** $l/H = 0.12$

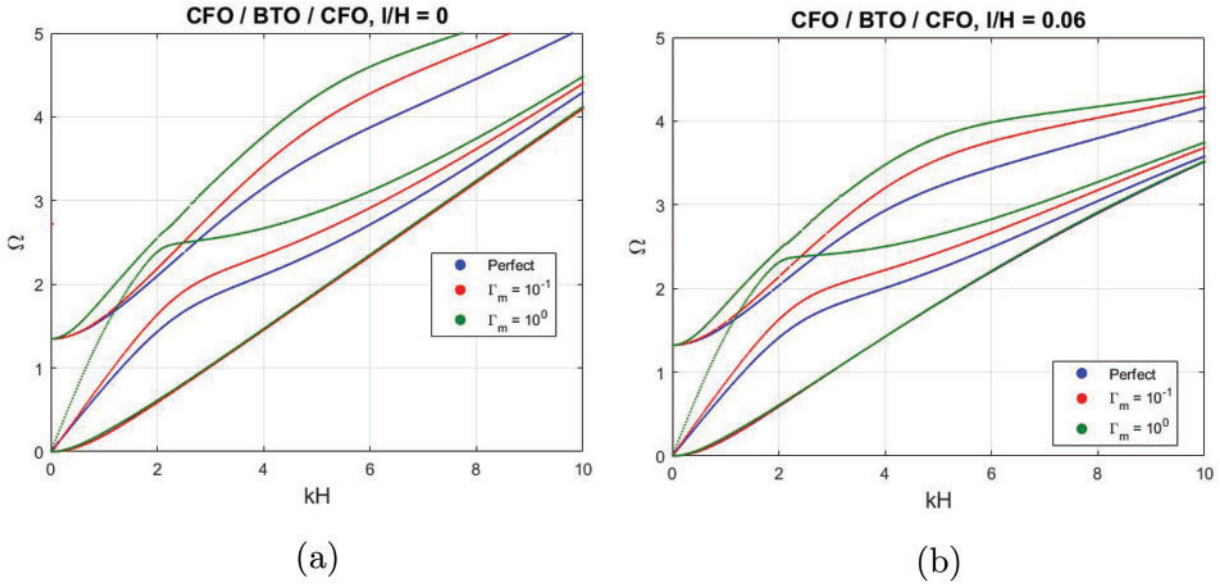

Figure 3: (Continued)

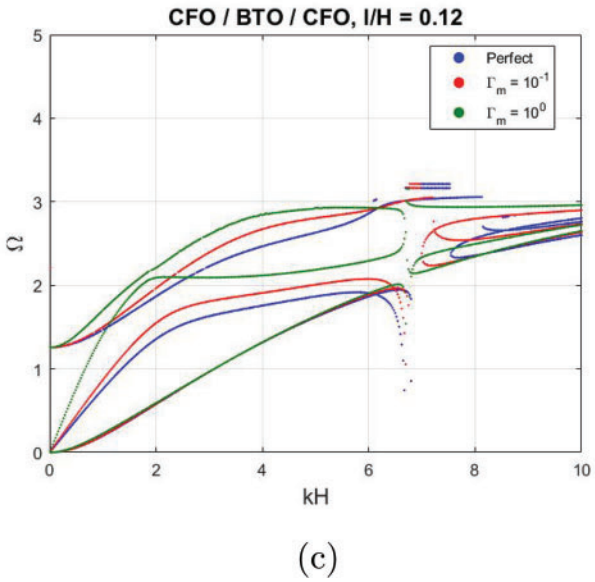

Figure 3: Dispersion curves for Lamb waves in a CFO/BTO/CFO sandwich plate with different interface contacts: perfect contact, imperfect contact with the relative scaling parameter $\Gamma_m = 10^{-1}$, $\Gamma_m = 10^0$. Dimensionless nonlocal length parameter **(a)** $l/H = 0$, **(b)** $l/H = 0.06$, **(c)** $l/H = 0.12$

Furthermore, the dispersion curves exhibited distinct discontinuities at specific wavenumber values $kH \approx 6$, 6.5, and 6.8 (Fig. 2c) and $kH \approx 6.8$, 7.5, and 8.1 (Fig. 3c). Analysis revealed that these discontinuities represented fundamentally different phenomena-the discontinuities at $kH \approx 6$, 6.5 (Fig. 2c) and 7.5, 8.1 (Fig. 3c) corresponded to abrupt phase velocity jumps. In contrast, the discontinuity at $kH \approx 6.8$ manifested as a rapid phase velocity variation. These discontinuities appeared in both perfect and imperfect interface conditions when the normalized nonlocal length reached $l/H = 0.12$. This indicates their origin is nonlocal effects rather than the interface imperfections.

We further investigated the modal natural frequencies associated with different nonlocal lengths and interface imperfections at a given wavenumber. Tables 1 and 2 present the first three modal natural frequencies at wavenumber $kH = 2$ for nonlocal BTO/CFO/BTO and CFO/BTO/CFO sandwich plate configurations. The results demonstrated significant interface effects-imperfect contact consistently produced higher frequencies at the examined wavenumber. This frequency elevation correlated directly with increasing interphase stiffness and strength, confirming that dimensionless natural frequencies increase with enhanced interfacial properties.

Table 1: Normalized natural frequencies of Lamb wave at $kH = 2$ in a BTO/CFO/BTO sandwich plate with various nonlocal lengths and interface conditions

Nonlocal length	Mode	Perfect	$\Gamma_m = 0.1$	$\Gamma_m = 1$
$l/H = 0$	1^{st}	0.5420	0.5561	0.5945
	2^{nd}	1.3810	1.5893	2.1330
	3^{rd}	1.9235	1.9876	2.1923
$l/H = 0.06$	1^{st}	0.5375	0.5513	0.5893
	2^{nd}	1.3645	1.5657	2.0621
	3^{rd}	1.8718	1.9311	2.1104
$l/H = 0.12$	1^{st}	0.5248	0.5376	0.5739
	2^{nd}	1.3182	1.4992	1.8760
	3^{rd}	1.7362	1.7828	1.9040

Table 2: Normalized natural frequencies of Lamb wave at $kH = 2$ in a CFO/BTO/CFO sandwich plate with various nonlocal lengths and interface conditions

Nonlocal length	Mode	Perfect	$\Gamma_m = 0.1$	$\Gamma_m = 1$
$l/H = 0$	1^{st}	0.5942	0.5988	0.6108
	2^{nd}	1.4324	1.6563	2.3864
	3^{rd}	2.0996	2.2071	2.5539
$l/H = 0.06$	1^{st}	0.5896	0.5941	0.6058
	2^{nd}	1.4127	1.6284	2.3116
	3^{rd}	2.0353	2.1402	2.4757
$l/H = 0.12$	1^{st}	0.5765	0.5806	0.5915
	2^{nd}	1.3571	1.5487	2.0914
	3^{rd}	1.8686	1.9668	2.2107

Figs. 4 and 5 show the first-order ($\Omega = \Omega_1$) and second-order mode ($\Omega = \Omega_2$) shapes along the thickness direction (y-axis) of the BTO/CFO/BTO plate at the given wavenumber $kH = 2$, evaluated at the fixed horizontal coordinate $(x, z) = (\pi/4, 0)$. Panels (a, b) show the elastic displacements u_1 and u_2; panels (c–f) illustrate the tractions σ_{21},σ_{22} and the stresses σ_{11},σ_{33}; and panels (g–h) show the electric displacement D_3 and magnetic flux density B_3. Figs. 6 and 7 illustrate the first-order and second-order mode shapes for the CFO/BTO/CFO plate configuration. The classical case results for the BTO/CFO/BTO plate configurations are consistent with those reported in a previous study [26]. The analysis confirmed two key interfacial behaviors: (1) continuous displacements u_1 and u_2 across all interfaces and (2) discontinuous traction σ_{21} due to the extended interface stress imperfections. Further observations from the first-order mode shapes (Figs. 4 and 6) revealed the following features. First, the displacement u_1, traction σ_{22}, stresses σ_{11} and σ_{33}, electric displacement D_3, and magnetic flux density B_3 exhibited anti-symmetric distributions about the midplane, while the displacement u_2 and traction σ_{21} showed symmetric distributions. These patterns reflect both the symmetry of the sandwich plate and the extended traction free boundary conditions. Second, the displacement u_1 and stresses σ_{11},σ_{33} reached maximum magnitudes at the top and bottom surfaces, while the traction σ_{21} peaked at the midplane. The electric displacement D_3 (magnetic flux density B_3) reached maximum conditions at both the top and bottom surfaces (Figs. 4 and 6, respectively), while the magnetic flux density B_3 (electric displacement D_3) peaked at the material interfaces (Figs. 4 and 6, respectively).

Third, an increase in the relative scaling parameter Γ_m resulted in an increase in the displacement u_2, an increase in the discontinuities traction σ_{21} across the interfaces, and a decrease in the discontinuities in electric displacement D_3 and magnetic flux density B_3. As the nonlocal length l increased, the values of u_2, σ_{21} increased, and the discontinuity of σ_{21} across the interface became more pronounced. Fourth, the nonlocal length l exhibited a negligible effect on u_1, σ_{11}, σ_{22}, σ_{33}, D_3 and B_3, as indicated by their clustered mode shapes and parameter insensitivity. Fifth, comparative analysis revealed that imperfect contacts exhibited significantly greater influence on mode shapes than nonlocal effects.

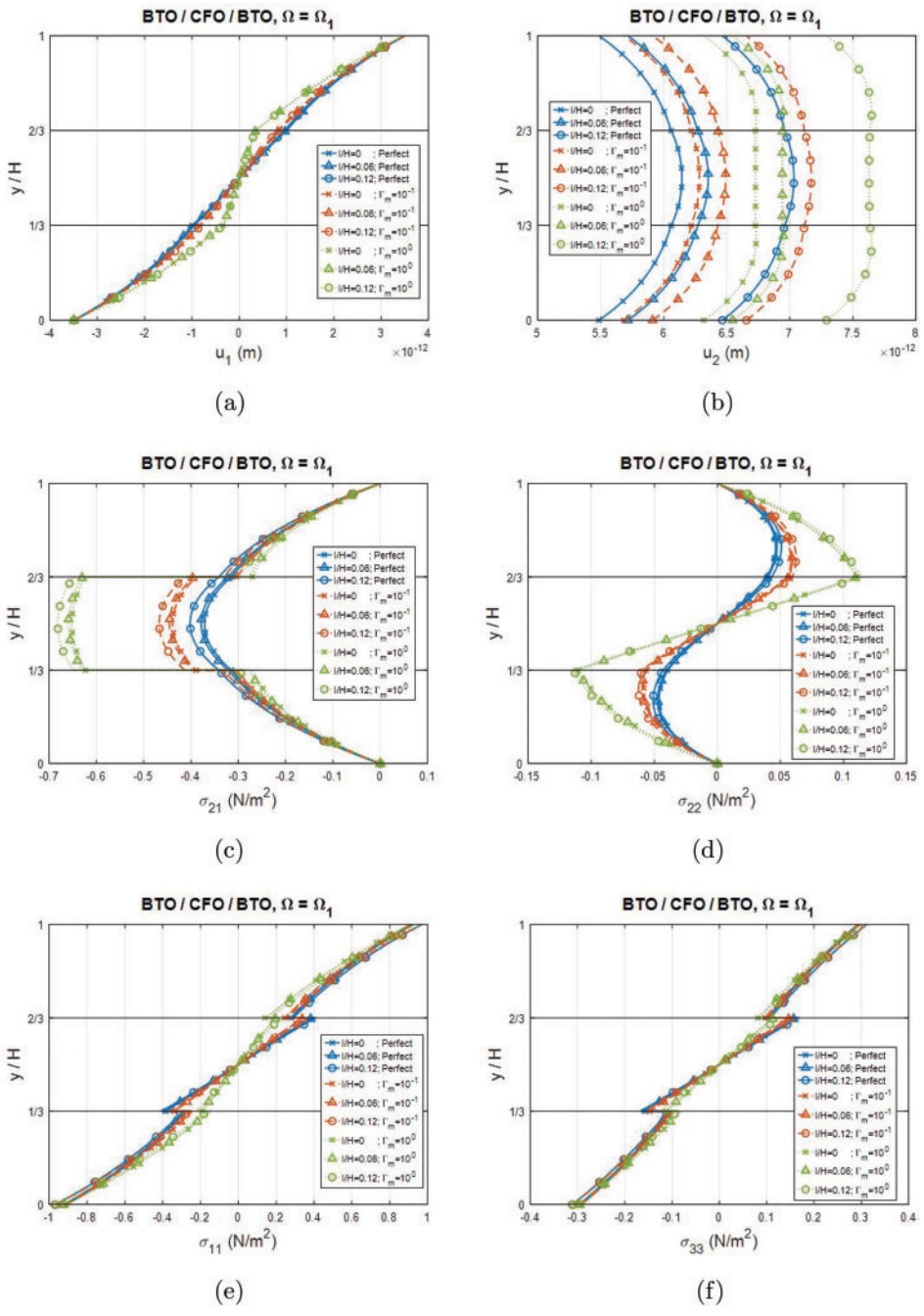

Figure 4: (Continued)

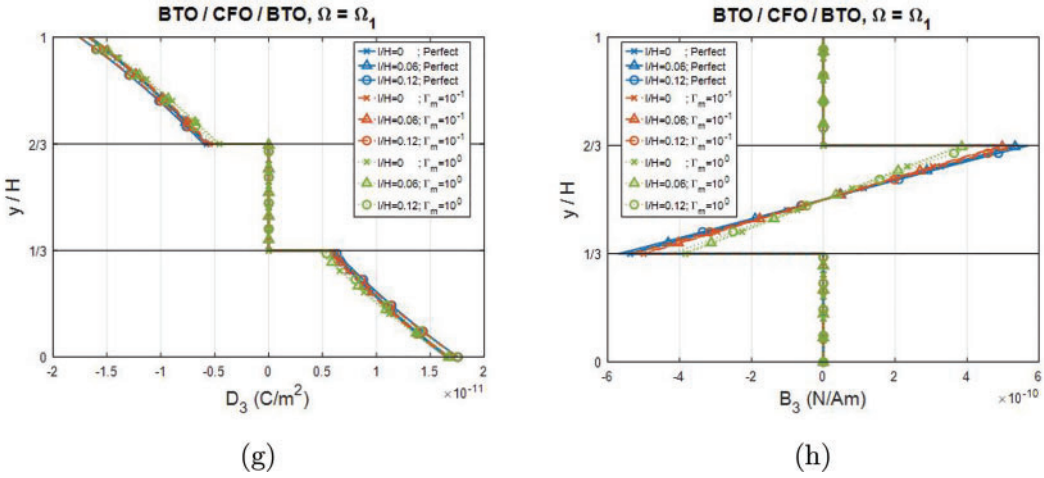

Figure 4: Variations for the first-order mode shapes of the Lamb wave in a BTO/CFO/BTO plate along the thickness direction (dimensionless wavenumber $kH = 2$): (a, b) displacements u_1 and u_2, (c, d) tractions σ_{21} and σ_{22}, (e–h) stresses σ_{11} and σ_{33}, electric displacement D_3, and magnetic flux density B_3. The plate is with nonlocal effect and extended interface stress imperfect interfaces

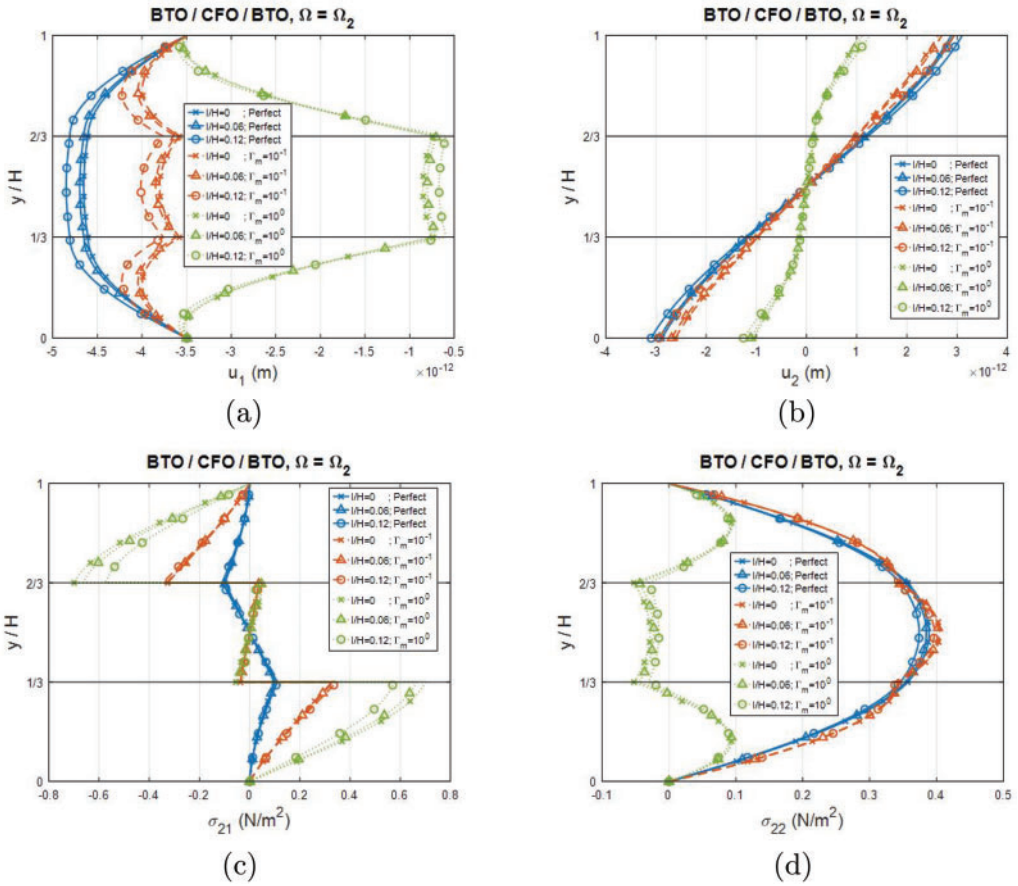

Figure 5: (Continued)

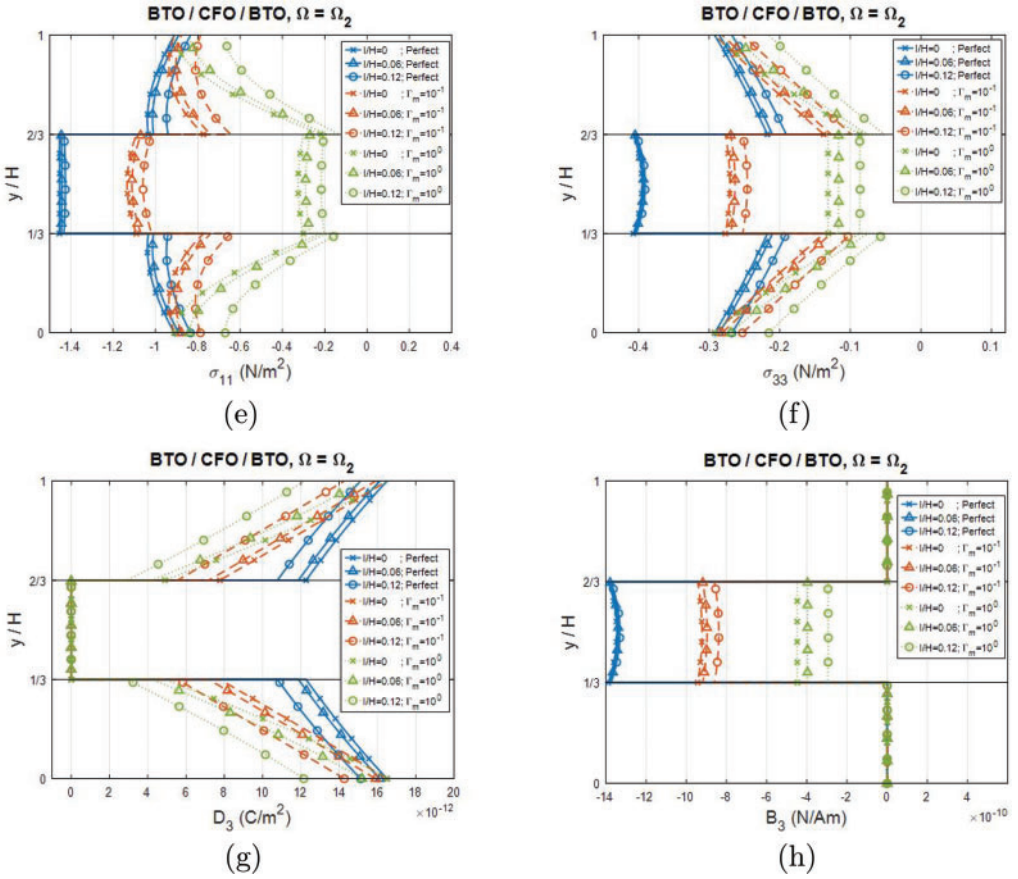

Figure 5: Variations for the second-order mode shapes of the Lamb wave in a BTO/CFO/BTO plate along the thickness direction (dimensionless wavenumber $kH = 2$): (a, b) displacements u_1 and u_2, (c, d) tractions σ_{21} and σ_{22}, (e–h) stresses σ_{11} and σ_{33}, electric displacement D_3, and magnetic flux density B_3. The plate is with nonlocal effect and extended interface stress imperfect interfaces

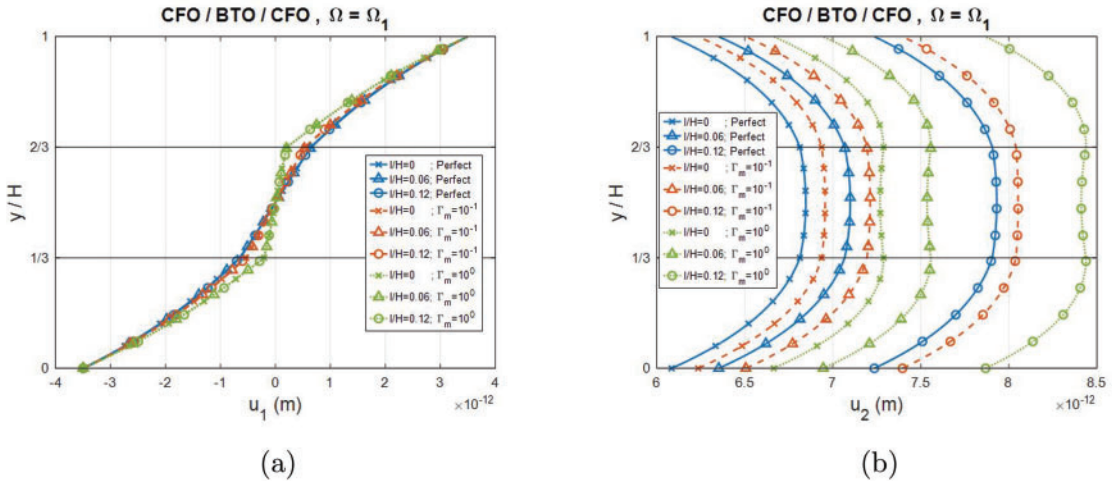

Figure 6: (Continued)

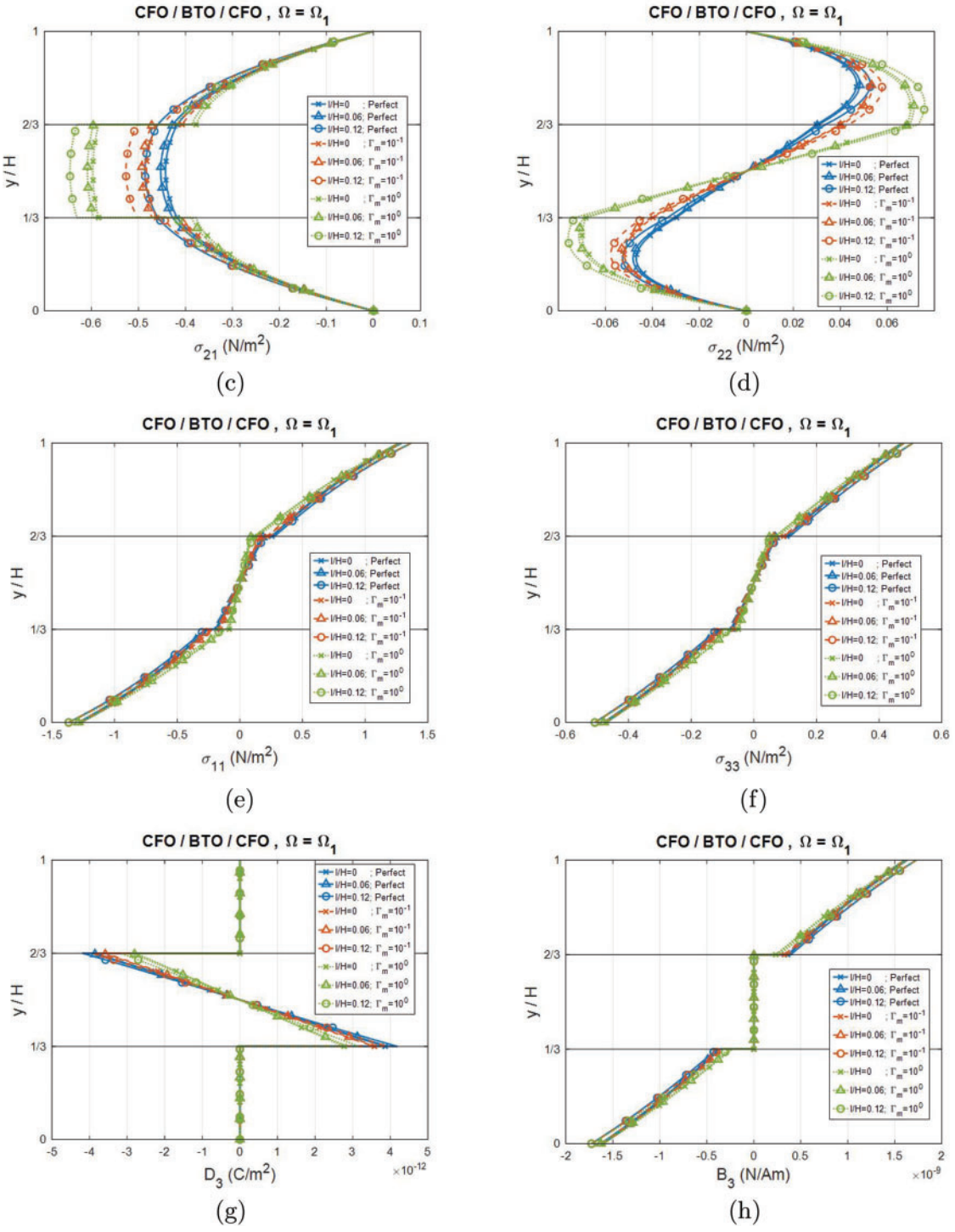

Figure 6: Variations for the first-order mode shapes of the Lamb wave in a CFO/BTO/CFO plate along the thickness direction (dimensionless wavenumber $kH = 2$): (a, b) displacements u_1 and u_2, (c, d) tractions σ_{21} and σ_{22}, (e–h) stresses σ_{11} and σ_{33}, electric displacement D_3, and magnetic flux density B_3. The plate is with nonlocal effect and extended interface stress imperfect interfaces

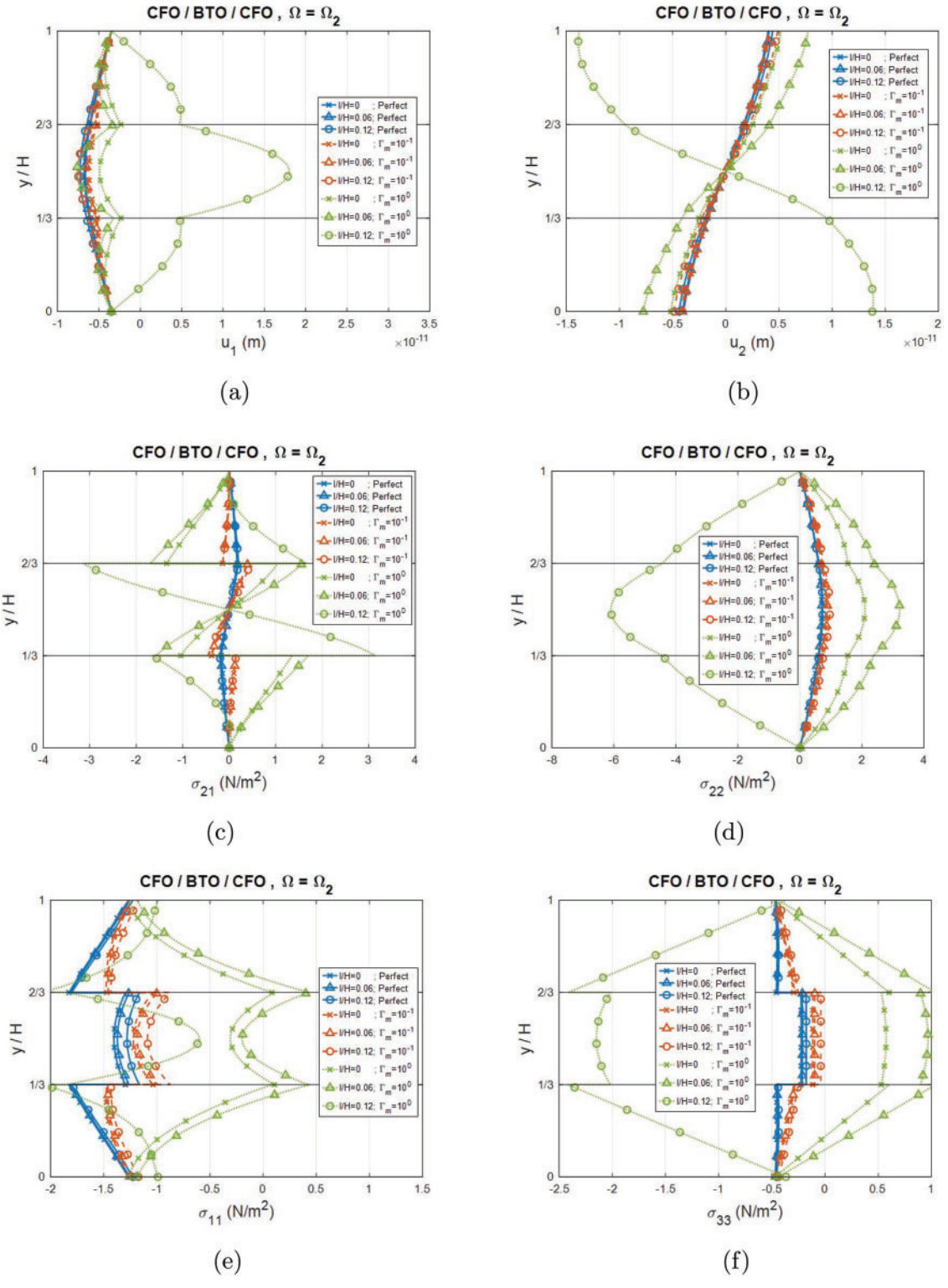

Figure 7: (Continued)

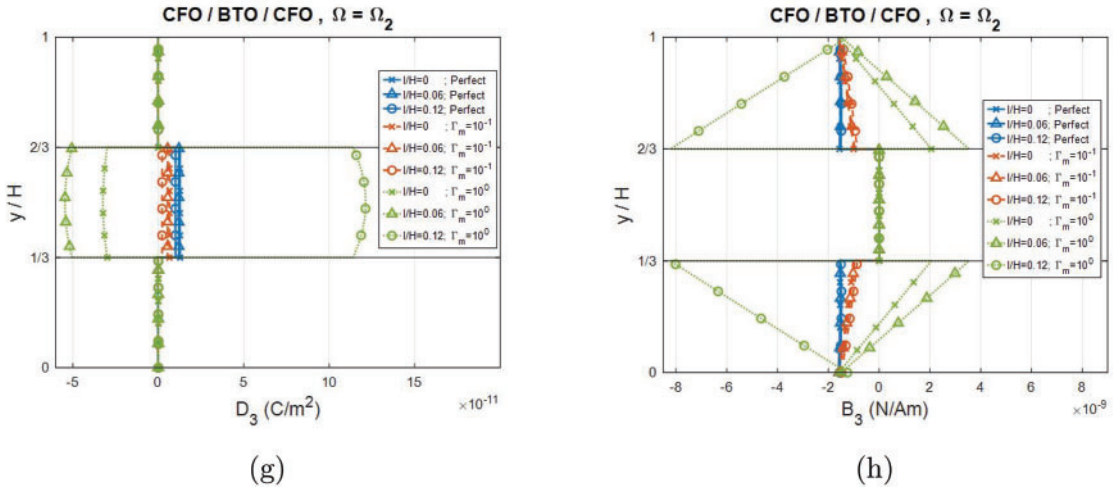

Figure 7: Variations for the second-order mode shapes of the Lamb wave in a CFO/BTO/CFO plate along the thickness direction (dimensionless wavenumber $kH = 2$): (a, b) displacements u_1 and u_2, (c, d) tractions σ_{21} and σ_{22}, (e–h) stresses σ_{11} and σ_{33}, electric displacement D_3, and magnetic flux density B_3. The plate is with nonlocal effect and extended interface stress imperfect interfaces

Analysis of the corresponding second-order mode shapes (Figs. 5 and 7), revealed consistent pattern for both configurations: (1) The displacement u_1, stresses σ_{11}, σ_{22}, σ_{33}, electric displacement D_3, and magnetic flux density B_3 exhibited symmetric distributions about the midplane, while the displacement u_2 and traction σ_{21} showed anti-symmetric behavior. (2) The displacement u_2 reached maximum magnitudes at both the top and bottom surfaces of the plate, while the traction σ_{21},stress σ_{33}, and magnetic flux density B_3 peaked at material interfaces. For the BTO/CFO/BTO plate configuration, we observed the following: (1) The relative scaling parameter Γ_m inversely affected interfacial discontinuities: increasing Γ_m decreased jumps in σ_{11}, σ_{33}, D_3 and B_3, while increasing the σ_{21} discontinuity. (2) Increasing the nonlocal lengths l decreased σ_{21},σ_{11}, σ_{33}, along with the interface discontinuities in D_3 and B_3. (3) The displacement u_2 and traction σ_{22} showed minimal sensitivity to nonlocal effects, as indicated by clustered mode shapes in the parameter space. (4) Imperfect contacts dominated over the nonlocal effects in modifying mode shapes. (5) The extended interface stress conditions induced polarity reversal in traction σ_{21} and σ_{22} fields. In contrast, the nonlocal length showed no polarity-reversal effects. For the CFO/BTO/CFO plate configuration, except the stress σ_{11}, all the remaining field components underwent directional reversal when both conditions were met: relative scaling parameter $\Gamma_m = 10^0$ and nonlocal length $l = 0.12$.

4.2 Love Wave

Figs. 8 and 9 show the variation of the first three dispersion curves for the Love wave in the BTO/CFO/BTO and CFO/BTO/CFO sandwich plate configurations under different nonlocal lengths and interfacial contact conditions. The analysis revealed that nonlocal effects significantly reduced dispersion values, particularly in high-frequency regimes (characterized by large wavenumbers and short wavelengths). Additionally, the nonlocal length modifications significantly altered the overall trend of the dispersion curves. The dispersion curves converged more rapidly as the nonlocal length increased. An increase in the nonlocal length resulted in a decrease in the slope of the curves. Furthermore, the effect of the interfacial imperfection was significant (Tables 3 and 4) for selected points at a wavenumber of $kH = 2$

in the BTO/CFO/BTO and CFO/BTO/CFO sandwich plates, respectively. The identical response patterns observed for both Love and Lamb waves indicated that the nonlocal constitutive law (1), rather than wave vibration type, primarily regulated dispersion characteristics.

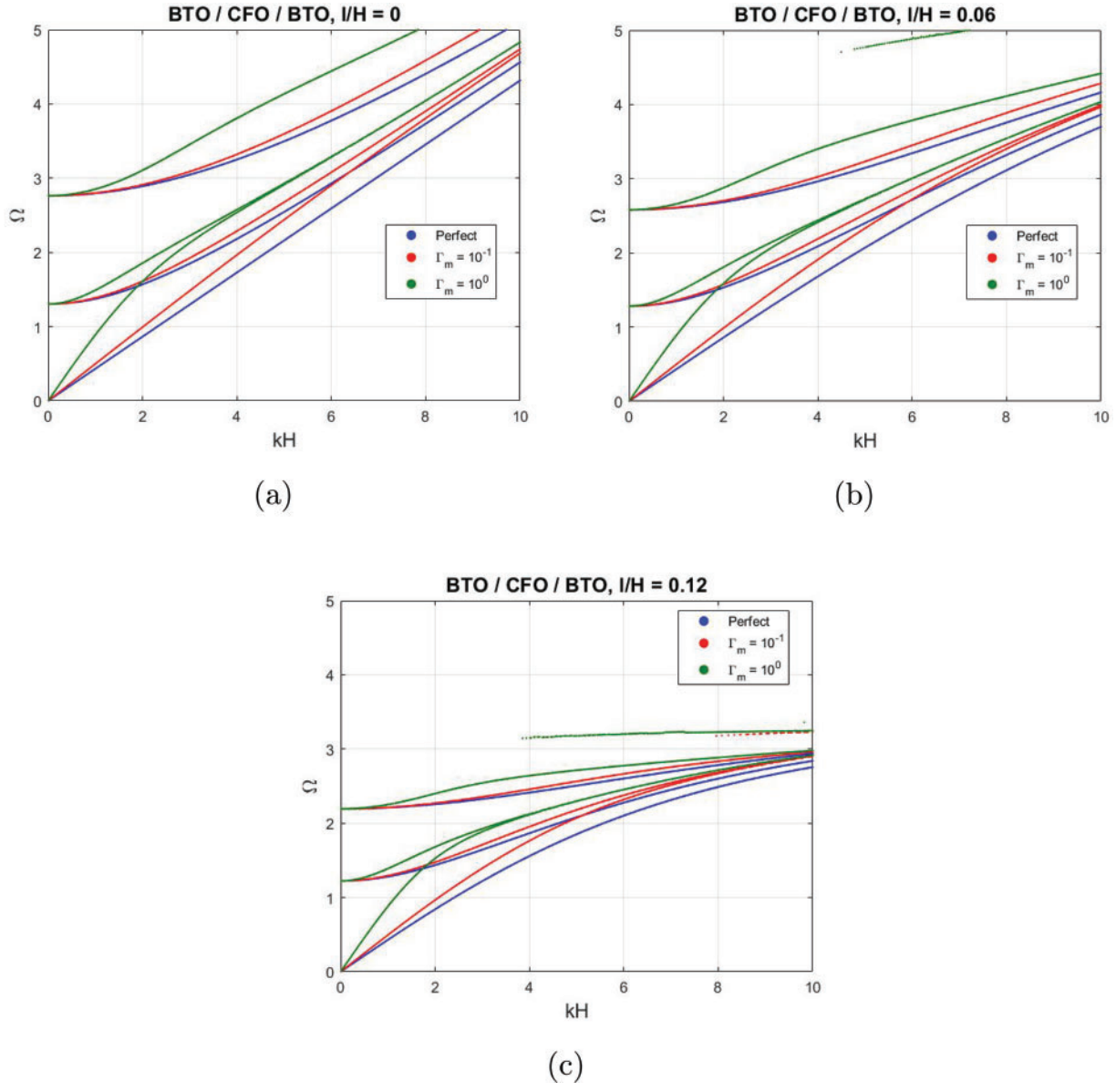

Figure 8: Dispersion curves for Love waves in a BTO/CFO/BTO sandwich plate with different interface contacts: perfect contact, imperfect contact with the relative scaling parameter $\Gamma_m = 10^{-1}$, $\Gamma_m = 10^{0}$. Dimensionless nonlocal length parameter (a) $l/H = 0$, (b) $l/H = 0.06$, (c) $l/H = 0.12$

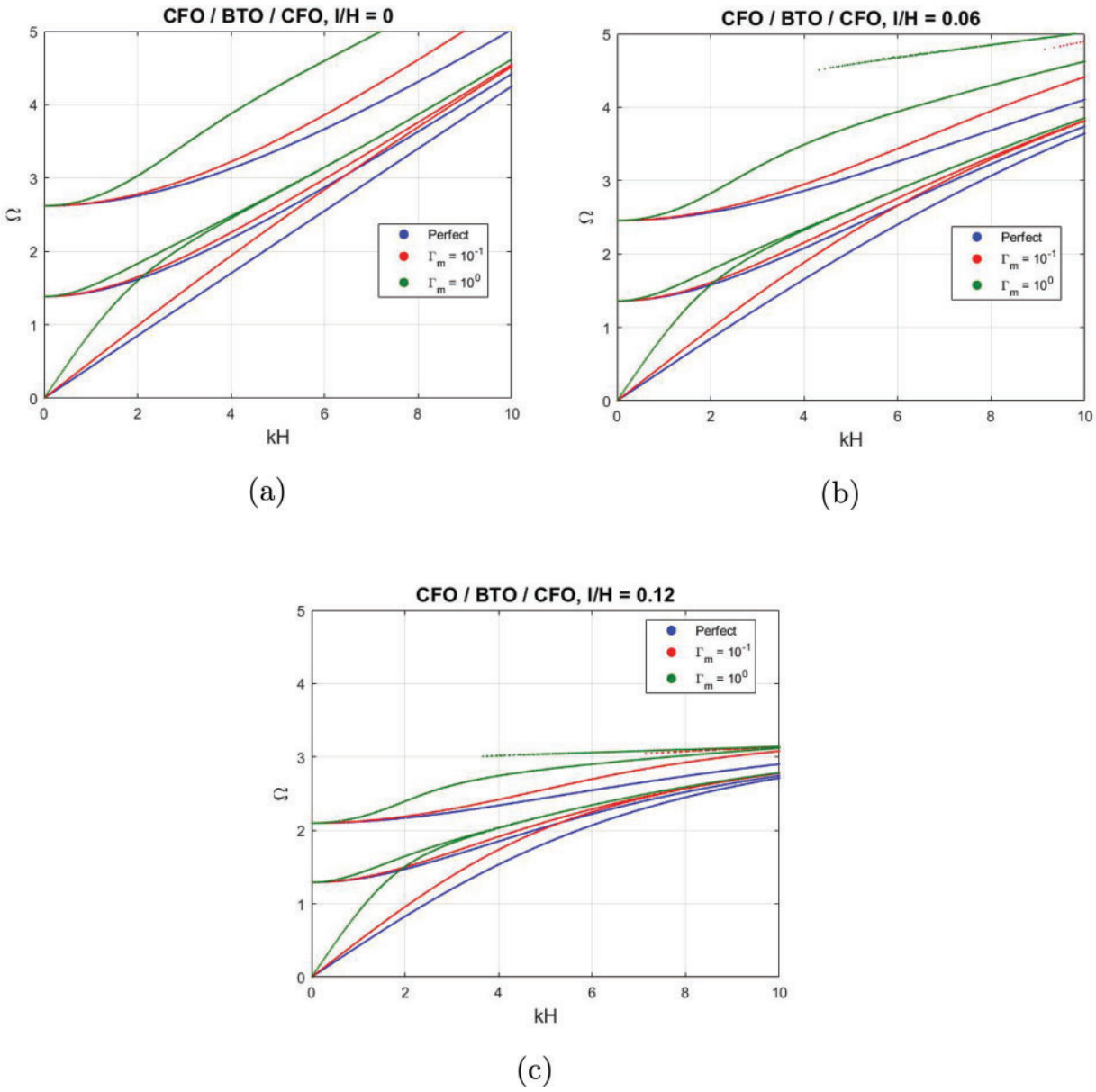

Figure 9: Dispersion curves for Love waves in a CFO/BTO/CFO sandwich plate with different interface contacts: perfect contact, imperfect contact with the relative scaling parameter $\Gamma_m = 10^{-1}$, $\Gamma_m = 10^{0}$. Dimensionless nonlocal length parameter (a) l/H= 0, (b) l/H = 0.06, (c) l/H = 0.12

Table 3: Normalized natural frequencies of Love wave at $kH = 2$ in a BTO/CFO/BTO sandwich plate with various nonlocal lengths and interface conditions

Nonlocal length	Mode	Perfect	$\Gamma_m = 0.1$	$\Gamma_m = 1$
$l/H = 0$	1^{st}	0.8646	0.9927	1.6087
	2^{nd}	1.5695	1.6113	1.8557
	3^{rd}	2.8924	2.9124	3.1062
$l/H = 0.06$	1^{st}	0.8584	0.9856	1.5877
	2^{nd}	1.5329	1.5738	1.8076
	3^{rd}	2.6850	2.7032	2.8776
$l/H = 0.12$	1^{st}	0.8407	0.9650	1.5258
	2^{nd}	1.4369	1.4754	1.6814
	3^{rd}	2.2570	2.2713	2.4003

Table 4: Normalized natural frequencies of Lamb wave at $kH = 2$ in a CFO/BTO/CFO sandwich plate with various nonlocal lengths and interface conditions

Nonlocal length	Mode	Perfect	$\Gamma_m = 0.1$	$\Gamma_m = 1$
$l/H = 0$	1^{st}	0.8512	0.9858	1.5978
	2^{nd}	1.6188	1.6499	1.8327
	3^{rd}	2.7557	2.7806	3.0295
$l/H = 0.06$	1^{st}	0.8451	0.9787	1.5748
	2^{nd}	1.5784	1.6085	1.7812
	3^{rd}	2.5661	2.5896	2.8256
$l/H = 0.12$	1^{st}	0.8276	0.9581	1.5066
	2^{nd}	1.4733	1.5008	1.6472
	3^{rd}	2.1695	2.1903	2.3971

Figs. 10 and 11 illustrate thickness-wise distributions of the first-order and second-order mode shapes of the BTO/CFO/BTO plate at a wavenumber $kH = 2$, respectively. Panels (a–c) show the elastic displacement u_3, electric potential ϕ, and magnetic potential ψ. Panels (d–f) show the shear stresses σ_{13}, σ_{23}, electric displacements D_1, D_2 and magnetic flux densities B_1, B_2, respectively. Figs. 12 and 13 illustrate the corresponding mode shapes for the CFO/BTO/CFO plate. Analysis of first-order mode shapes (Figs. 10 and 12) revealed seven key characteristics: (1) The displacement u_3, electric potential ϕ, and magnetic potential ψ remained continuous across the imperfect interfaces, while the traction σ_{23}, normal electric displacement D_2, and magnetic flux density B_2 exhibited discontinuities. (2) The distributions of u_3,ϕ, ψ, σ_{13}, D_1, and B_1 were symmetric about the midplane, while σ_{23}, D_2, and B_2 showed anti-symmetric behavior. (3) The traction σ_{23}, electric displacement D_1, D_2, magnetic flux density B_1 and B_2 reached their maximum values at the interfaces. (4) An increase in the relative scaling parameter Γ_m resulted in an increase of σ_{23}, D_2 and B_2. This occurred due to the increasing the interface stiffness (or equivalently, the relative scaling parameter Γ_m) enhanced the discontinuity in σ_{23}, D_2 and B_2 across the interface under the interface stress model. (5) An increase in the nonlocal length l resulted in a decrease in u_3, σ_{13}, σ_{23}, D_1, D_2, B_1, and B_2. (6) The nonlocal length l exhibited a minimal effect on the distribution of ϕ and ψ. The corresponding mode shapes were clustered, indicating insensitivity to the nonlocal length. (7) Compared to the effect of imperfect conditions, the influence of the nonlocal length on the mode shape distributions was less significant.

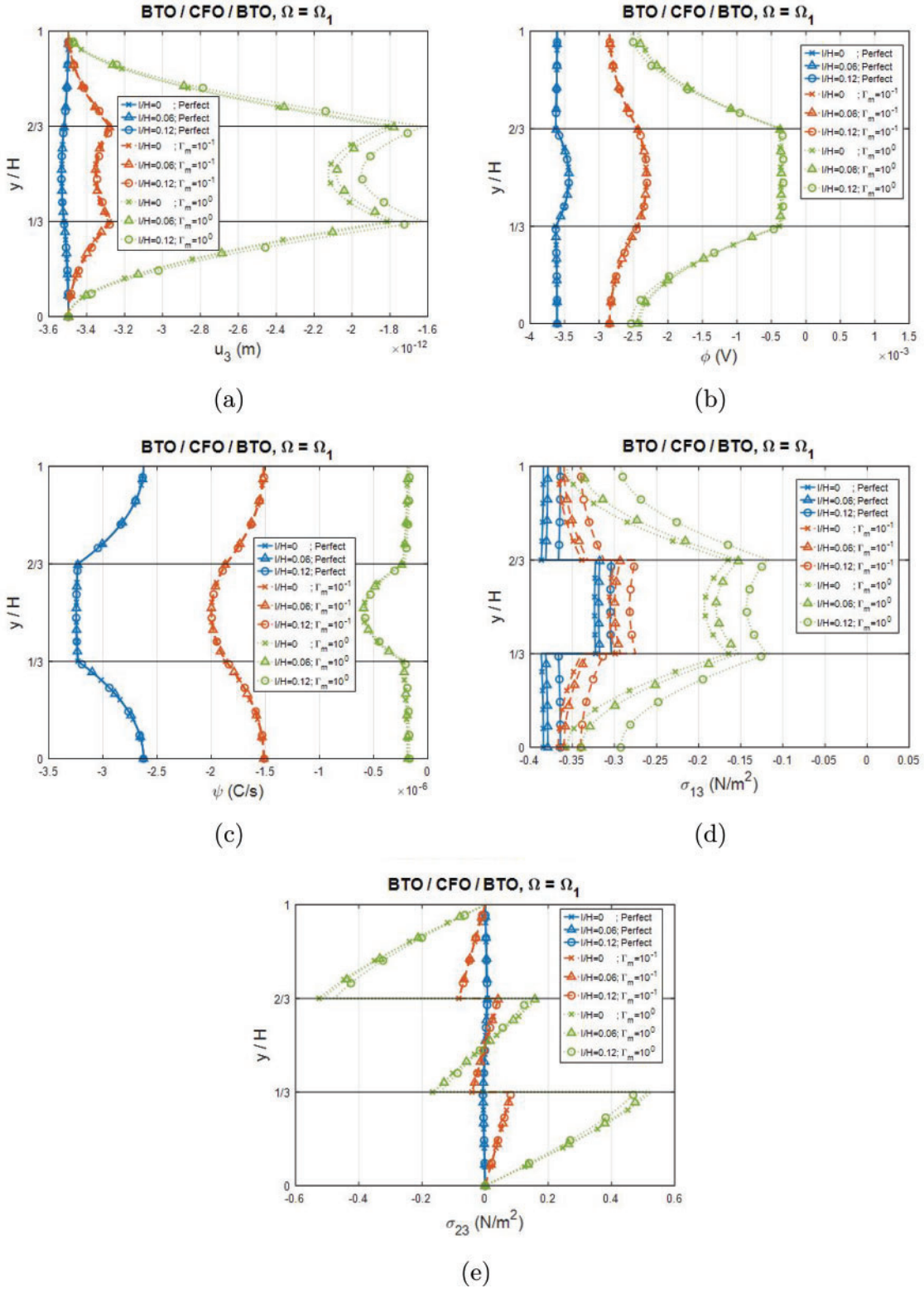

Figure 10: (Continued)

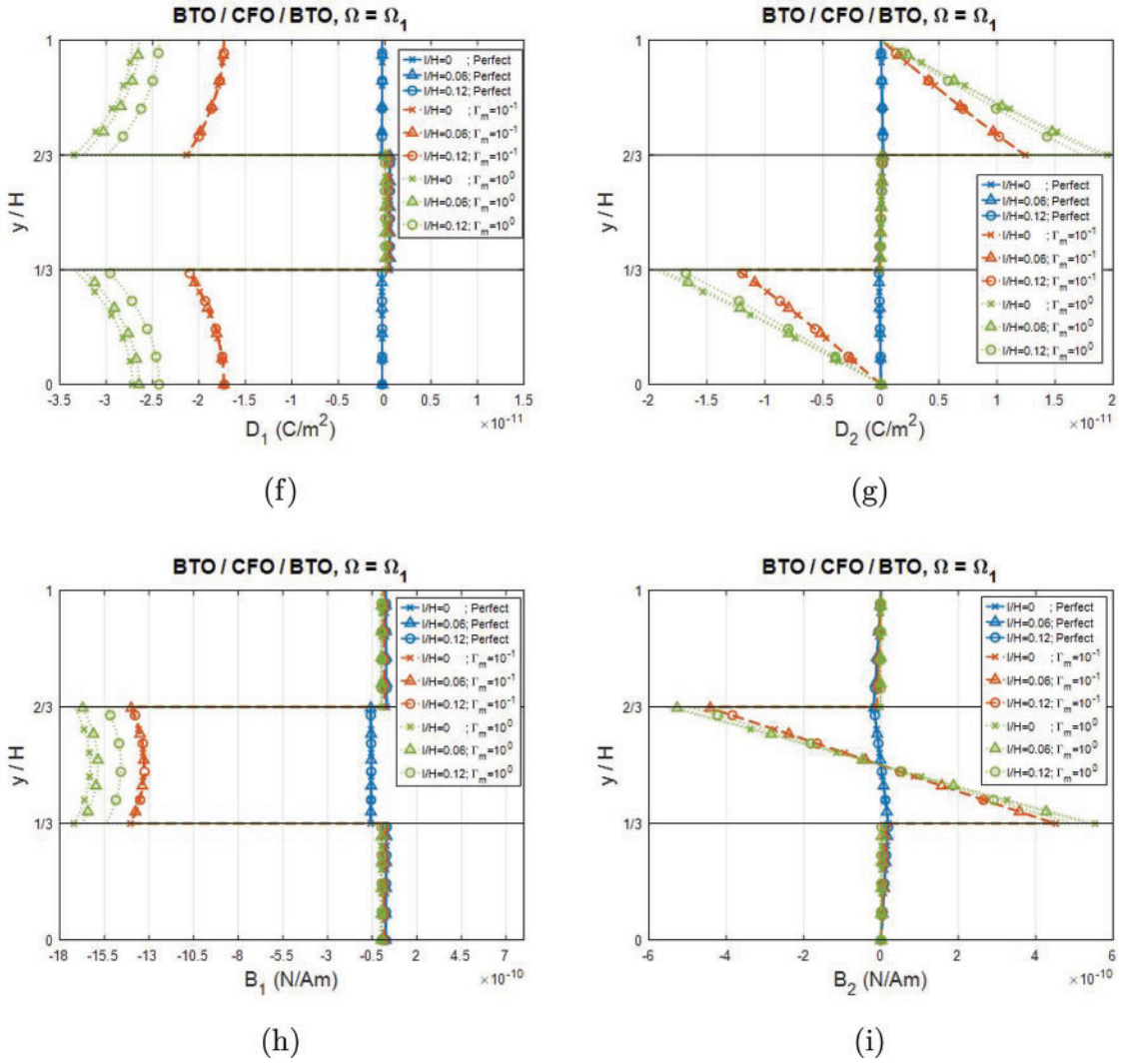

Figure 10: Variations for the first-order mode shapes of the Love wave in a BTO/CFO/BTO plate along the thickness direction (dimensionless wavenumber kH = 2): (a–c) displacement u_3, electric potential ϕ, and magnetic potential ψ, (d,e) stresses σ_{13} and σ_{23}, (f,g) electric displacements D_1 and D_2, (h,i) magnetic flux density B_1 and B_2. The plate is with nonlocal effect and extended interface stress imperfect interfaces

For the second-order mode shapes (Figs. 11 and 13), the following features were observed for both plate configurations: (1) The distributions of u_3,ϕ, ψ, σ_{13}, D_1 and B_1 were anti-symmetric about the midplane, while the extended tractions σ_{23}, D_2, and B_2 were symmetric about the midplane. (2) The fields of u_3, σ_{13} reached their maximum values at both the top and bottom surfaces, while the fields of D_1, D_2, B_1 and B_2 peaked at the interfaces. (3) An increase in the relative scaling parameter Γ_m resulted in a decrease of u_3, ϕ, ψ, and σ_{13} and an increase of the discontinuities of σ_{23}, D_1, D_2, B_1 and B_2 across the interfaces. (4) An increase in the nonlocal length l resulted in a decrease in σ_{13} and σ_{23}. (5) The nonlocal length l had negligible effects on u_3, ϕ, and ψ. The mode shapes of these field quantities were clustered, suggesting insensitivity to the nonlocal length parameter. (6) Compared to the extended interface stress conditions, the effects of the nonlocal length on the mode shape distributions were less significant.

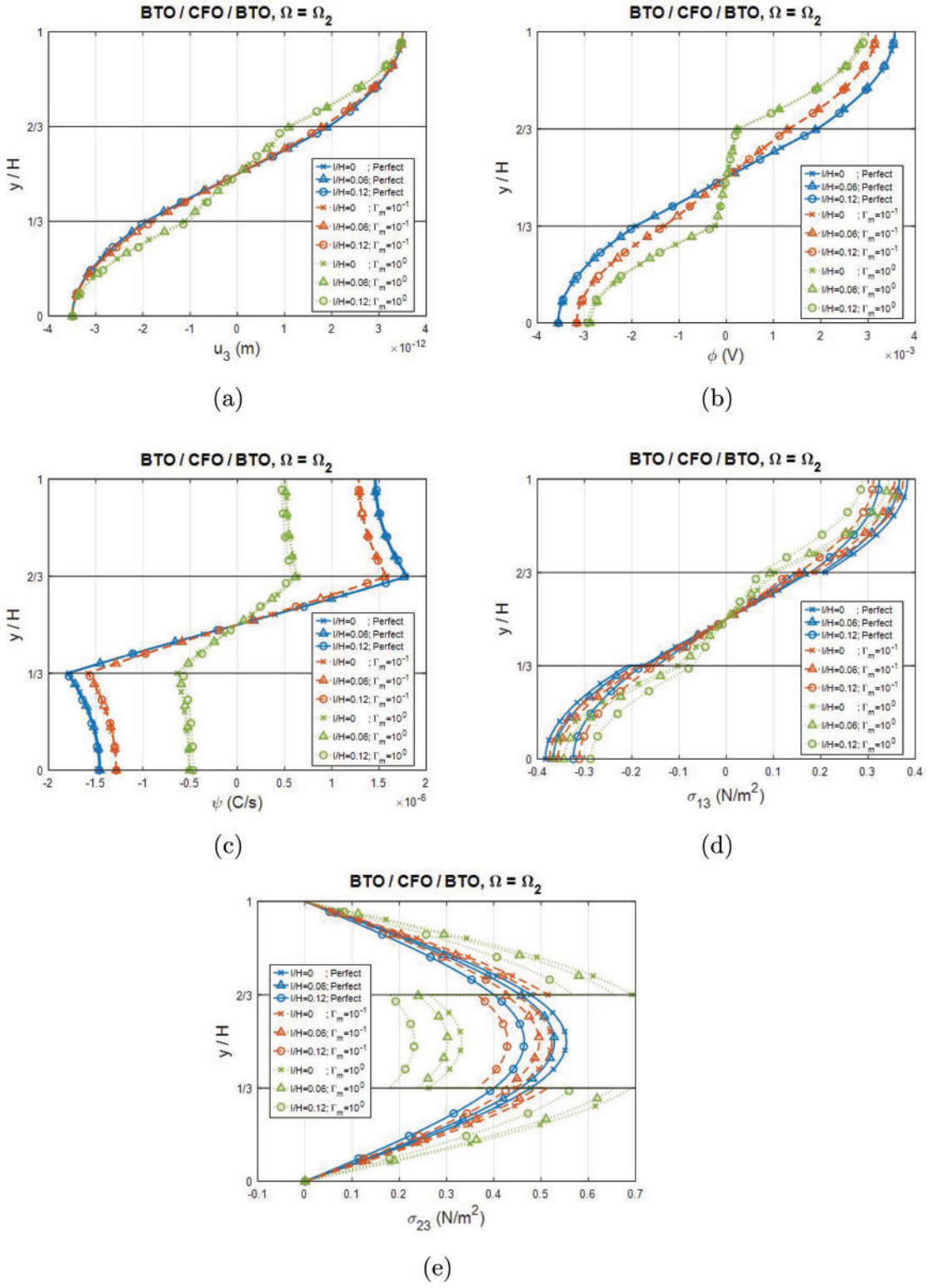

Figure 11: (Continued)

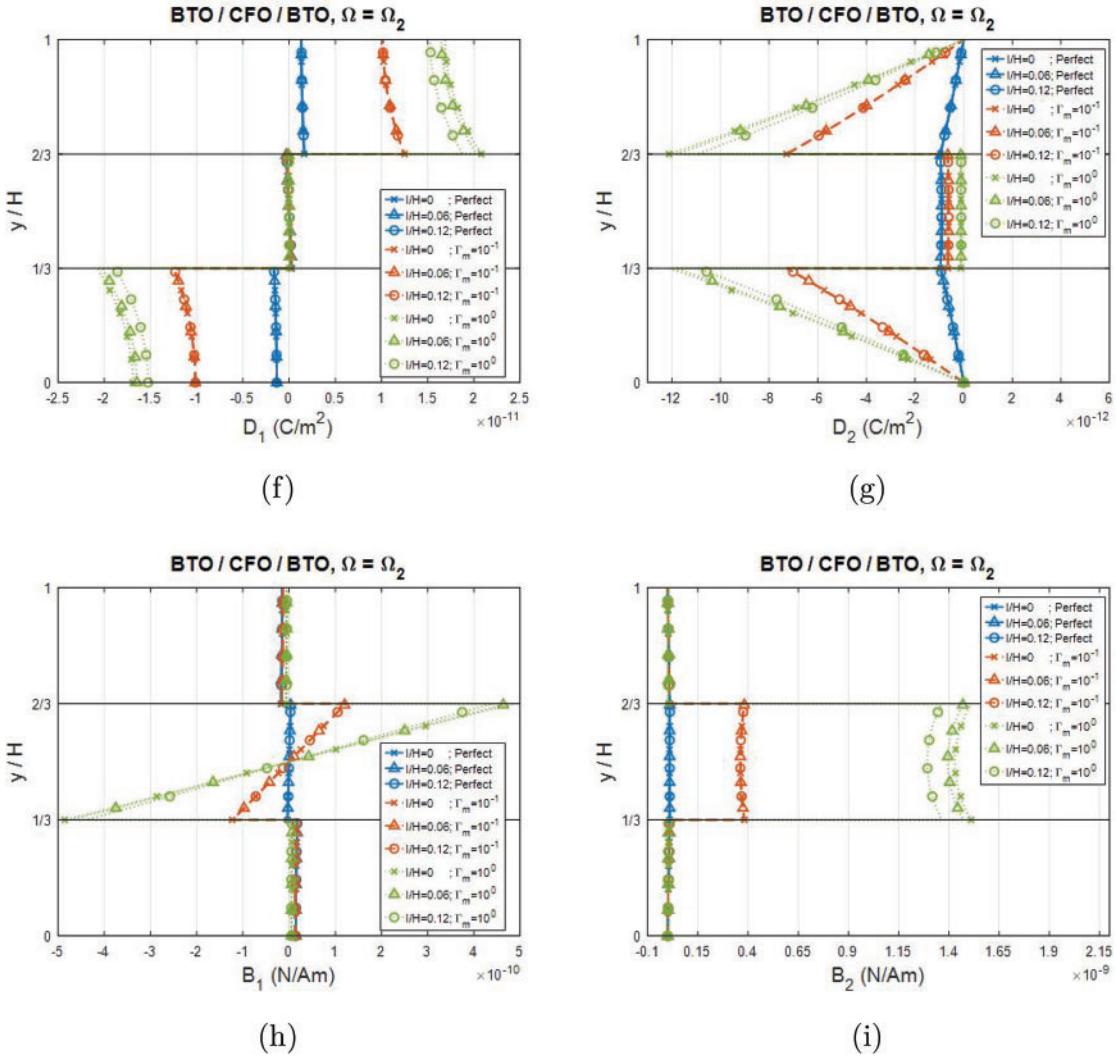

Figure 11: Variations for the second-order mode shapes of the Love wave in a BTO/CFO/BTO plate along the thickness direction (dimensionless wavenumber $kH = 2$): (a–c) displacement u_3, electric potential ϕ, and magnetic potential ψ, (d,e) stresses σ_{13} and σ_{23}, (f,g) electric displacements D_1 and D_2, (h,i) magnetic flux density B_1 and B_2. The plate is with nonlocal effect and extended interface stress imperfect interfaces

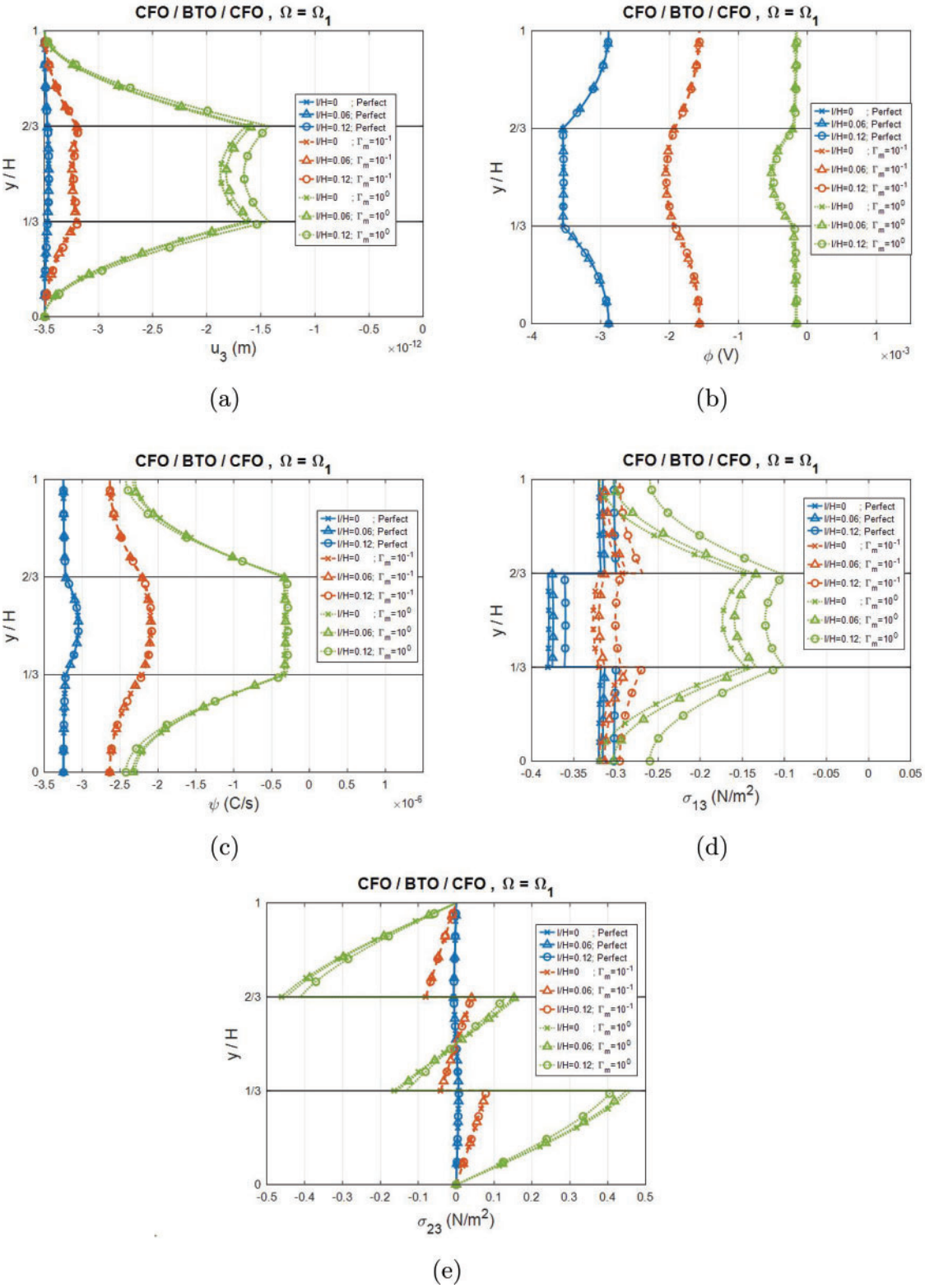

Figure 12: (Continued)

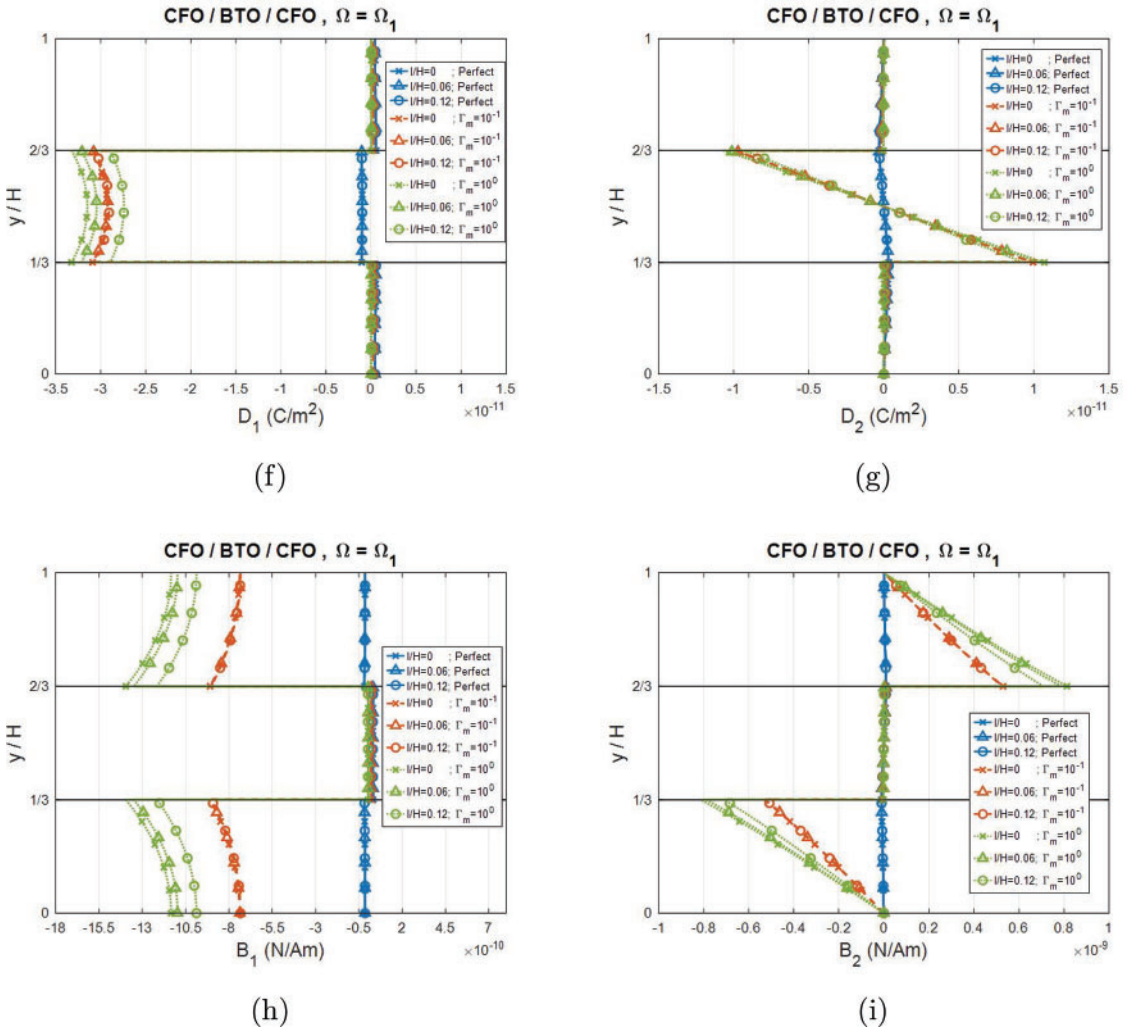

Figure 12: Variations for the first-order mode shapes of the Love wave in a CFO/BTO/CFO plate along the thickness direction (dimensionless wavenumber $kH = 2$): (a–c) displacement u_3, electric potential ϕ, and magnetic potential ψ, (d,e) stresses σ_{13} and σ_{23}, (f,g) electric displacements D_1 and D_2, (h,i) magnetic flux density B_1 and B_2. The plate is with nonlocal effect and extended interface stress imperfect interfaces

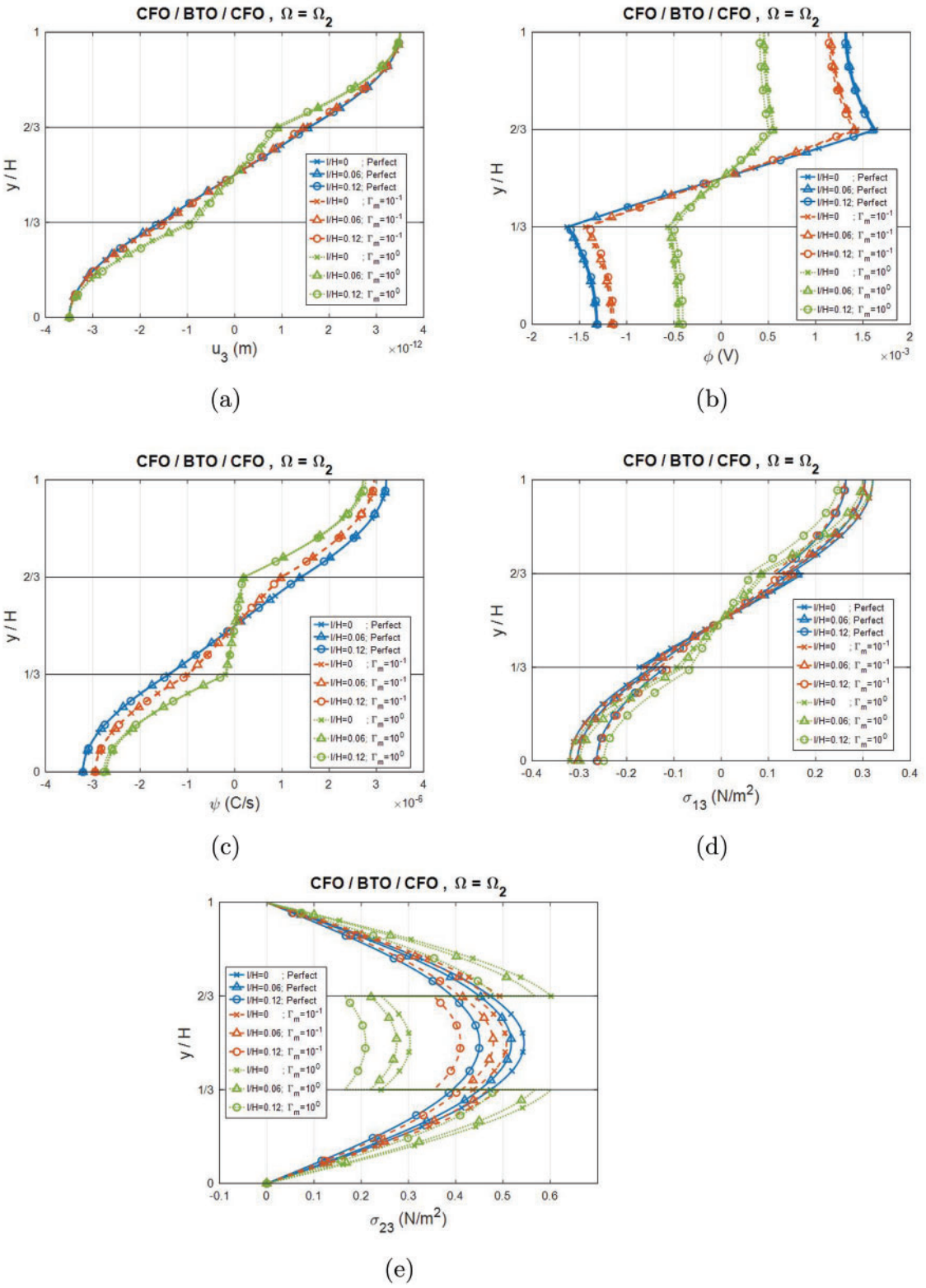

Figure 13: (Continued)

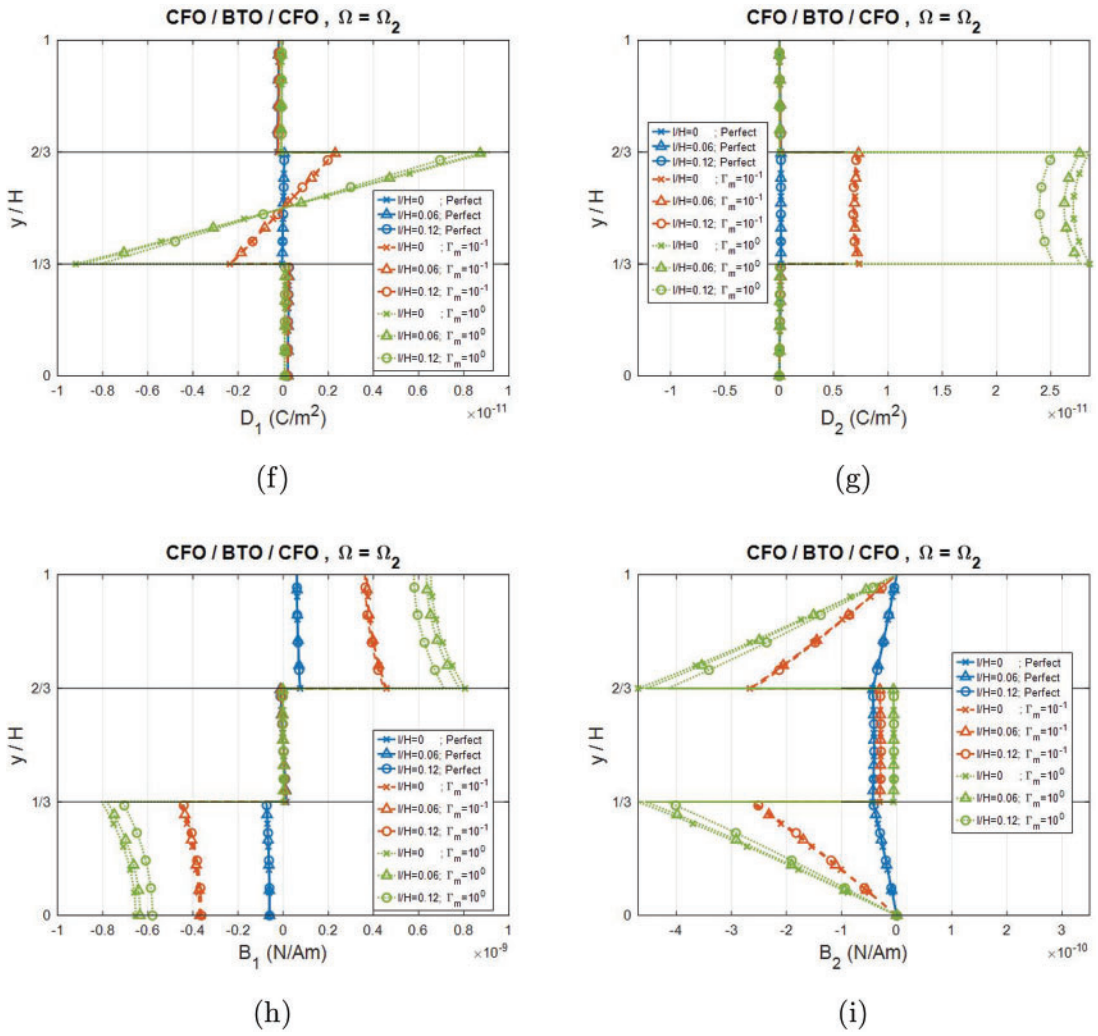

Figure 13: Variations for the second-order mode shapes of the Love wave in a CFO/BTO/CFO plate along the thickness direction (dimensionless wavenumber $kH = 2$): (a–c) displacement u_3, electric potential ϕ, and magnetic potential ψ, (d,e) stresses σ_{13} and σ_{23}, (f,g) electric displacements D_1 and D_2, (h,i) magnetic flux density B_1 and B_2. The plate is with nonlocal effect and extended interface stress imperfect interfaces

5 Conclusions

In this study, a comprehensive analytical framework was developed for predicting three-dimensional field distributions in nonlocal MEE laminates with interface stress imperfections. The methodology was used to generalize four key components: the pseudo-Stroh formulation, transfer matrix method, interface matrix method, and the nonlocal constitutive equation proposed by Eringen, which were collectively facilitate recursive field solutions. The key theoretical advancement involved the constructive relationship between the nonlocal and classical extended tractions fields. The analytical framework was illustrated through its application to BTO/CFO/BTO and CFO/BTO/CFO sandwich plates. The study revealed the following key findings: (1) both the nonlocal effect and interface stress-type imperfections significantly influenced the dispersion curves; (2) increasing the nonlocal length reduced the natural frequency, particularly in high-frequency regions; (3) increasing the severity of interface stress-type imperfections increases the natural frequency; (4) compared to the interface imperfections, the nonlocal effect has a less significant influence on

the mode shapes of most field quantities; (5) the mode shapes of some field quantities exhibit similar behavior and appear insensitive to variations in the nonlocal length parameter; (6) interface stress-type imperfections reverses the direction and enhances the magnitude of the mode shapes, with the nonlocal effect further amplifying these changes.

While the current model effectively captures the local behavior of the investigated plate, its applicability to more complex laminated nanostructures may be limited. Specifically, the formulation may require an extension to address piezomagnetic facesheet configurations or a CNT composite layer with piezoelectric surface layers (common in energy harvesting applications). Future studies should focus on extending this framework to investigate these advanced MEE plate configurations, incorporate higher-fidelity plate theories (e.g., layer-wise or zigzag models), and improve local field distribution predictions in composite architecture [33].

Acknowledgement: The author is grateful to the editor and anonymous referees for their insightful comments and suggestions, which helped to improve the paper's presentation.

Funding Statement: The study is supported by the Ministry of Science and Technology Taiwan under Grant No. MOST 109-2628-E-009-002-MY3.

Author Contributions: The authors confirm contribution to the paper as follows: study conception and design: Hsin-Yi Kuo; analysis and interpretation of results: Li-Huan Yang, Hsin-Yi Kuo; draft manuscript preparation: Li-Huan Yang, Hsin-Yi Kuo. All authors reviewed the results and approved the final version of the manuscript.

Availability of Data and Materials: All data that support the findings of this study are included within the article.

Ethics Approval: Not applicable.

Conflicts of Interest: The authors declare no conflicts of interest to report regarding the present study.

References

1. Eerenstein W, Mathur ND, Scott JF. Multiferroic and magnetoelectric materials. Nature. 2006;442(7104):759–65. doi:10.1038/nature05023.
2. Vinyas M. Computational analysis of smart magneto-electro-elastic materials and structures: review and classification. Arch Comput Method Eng. 2021;28(3):1205–48. doi:10.1007/s11831-020-09406-4.
3. Shetty S, Palkar VR, Pinto R. Size effect study in magnetoelectric $BiFeO_3$ system. J Phys. 2002;58(5–6):1027–30. doi:10.1007/s12043-002-0211-4.
4. Bühlmann S, Dwir B, Baborowski J, Muralt P. Size effect in mesoscopic epitaxial ferroelectric structures: increase of piezoelectric response with decreasing feature size. Appl Phys Lett. 2002;80(17):3195–7. doi:10.1063/1.1475369.
5. Yoo K, Jeon BG, Chun SH, Patil DR, Lim YJ, Noh SH, et al. Quantitative measurements of size-dependent magnetoelectric coupling in Fe_3O_4 nanoparticles. Nano Lett. 2016;16(12):7408–13. doi:10.1021/acs.nanolett.6b02978.
6. Eringen AC. On differential equations of nonlocal elasticity and solutions of screw dislocation and surface waves. J Appl Phys. 1983;54(9):4703–10. doi:10.1063/1.332803.
7. Eringen AC. Nonlocal continuum field theories. New York, NY, USA: Springer; 2002.
8. Di Paola M, Failla G, Pirrotta A, Zingales M. The mechanically based non-local elasticity: an overview of main results and future challenges. Philos Trans A. 2013;371(1993):20120433. doi:10.1098/rsta.2012.0433.
9. Wu C-P, Li W-C. Free vibration analysis of embedded single-layered nanoplates and graphene sheets by using the multiple time scale method. Computer Math Appl. 2017;73(5):838–54. doi:10.1016/j.camwa.2017.01.014.
10. Wu C-P, Yu J-Y. A review of mechanical analyses of rectangular nanobeams and single-, double-, and multi-walled carbon nanotubes using Eringen's nonlocal elasticity theory. Arch Appl Mech. 2019;89(9):1761–92. doi:10.1007/s00419-019-01542-z.

11. Ke L-L, Wang Y-S, Yang J, Kitipornchai S. Free vibration of size-dependent magneto-electro-elastic nanoplates based on the nonlocal theory. Acta Mech Sinica. 2014;30(4):516–25. doi:10.1007/s10409-014-0072-3.
12. Amiri A, Fakhari SM, Pournaki IJ, Rezazadeh G, Shabani R. Vibration analysis of circular magneto-electro-elastic nano-plates based on Eringen's nonlocal theory. Int J Eng Trans. 2015;C 28:1808–17.
13. Pan E, Waksmanski N. Deformation of a layered magnetoelectroelastic simply-supported plate with nonlocal effect, an analytical three-dimensional solution. Smart Mater Struct. 2016;25(9):095013. doi:10.1088/0964-1726/25/9/095013.
14. Waksmanski N, Pan E. An analytical three-dimensional solution for free vibration of a magneto-electro-elastic plate considering the nonlocal effect. J Intel Mater Syst Struct. 2017;28(11):1501–13. doi:10.1177/1045389x16672734.
15. Ke L-L, Wang Y-S, Yang J, Kitipornchai S. The size-dependent vibration of embedded magneto-electro-elastic cylindrical nanoshells. Smart Mater Struct. 2014;23(12):125036. doi:10.1088/0964-1726/23/12/125036.
16. Kuo H-Y. Effective moduli of multiferroic fibrous composites with strain gradient and electromagnetic field gradient effects. Int J Solids Struct. 2021;222–223:111007. doi:10.1016/j.ijsolstr.2021.02.018.
17. Li G-E, Kuo H-Y. Effects of strain gradient and electromagnetic field gradient on potential and field distributions of multiferroic fibrous composites. Acta Mech. 2021;232(4):1353–78. doi:10.1007/s00707-020-02910-5.
18. Liu C, Li. K, Min S, Chai Y. Dynamic analysis of the three-phase magneto-electro-elastic (MEE) structures with the overlapping triangular finite elements. Comput Math Appl. 2025;179:148–177.2. doi:10.1016/j.camwa.2024.11.025.
19. Jiang Z, Gui Q, Li W, Chai Y. Assessment of the edge-based smoothed finite element method for dynamic analysis of the multi-phase magneto-electro-elastic structures. Eng Anal Bound Elem. 2024;163(3):94–107. doi:10.1016/j.enganabound.2024.02.021.
20. Kuo H-Y, Yang L-H, Huang P-C, Pan E. Comparisons of wave characteristics in magneto-electro-elastic laminated composites with different layering directions. Acta Mech. 2023;234(9):4467–85. doi:10.1007/s00707-023-03611-5.
21. Ly D-K, Vu H-N, Thongchom C, Nguyen-Thoi T. A multi-physical coupling isogeometric formulation for nonlinear analysis and smart control of laminated CNT-MEE plates. Eng Anal Bound Elem. 2024;159(13):36–57. doi:10.1016/j.enganabound.2023.11.023.
22. Bichurin MI, Petrov VM, Srinivasan G. Theory of low-frequency magnetoelectric coupling in magnetostrictive-piezoelectric bilayers. Phys Rev B. 2003;68(5):054402. doi:10.1103/physrevb.68.054402.
23. Wang Y, Su Y, Li J, Weng GJ. A theory of magnetoelectric coupling with interface effects and aspect-ratio dependence in piezoelectric-piezomagnetic composites. J Appl Phys. 2015;117(16):164106. doi:10.1063/1.4919016.
24. Kuo H-Y, Chung C-Y. Multiferroic laminated composites with interfacial imperfections and the nonlocal effect. Compos Struct. 2022;287:115235. doi:10.1016/j.compstruct.2022.115235.
25. Kuo H-Y, Wang Y-H. Wave motion of magneto-electro-elastic laminated plates with membrane-type interfacial imperfections. Compos Struct. 2022;293:115661. doi:10.1016/j.compstruct.2022.115661.
26. Kuo H-Y, Huang P-C. Nonlocal free vibration of magneto-electro-elastic nanoplates with imperfect contacts. Mech Adv Mater Struct. 2024;31(30):12759–73. doi:10.1080/15376494.2024.2328753.
27. Dong S, Li J-F, Viehland D. Longitudinal and transverse magnetoelectric voltage coefficients of magnetostrictive/piezoelectric laminate composite: experiments. IEEE Trans Ultras, Ferroelectr Frequ Control. 2004;51(7):794–9. doi:10.1109/tuffc.2004.1320738.
28. Wang Y, Or SW, Chan HLW, Zhao Z, Luo H. Enhanced magnetoelectric effect in longitudinal-transverse mode Terfenol-D/Pb($Mg_{1/3}Nb_{2/3}$)O_3-$PbTiO_3$ laminate composites with optimal crystal cut. J Appl Phys. 2008;103(12):124511. doi:10.1063/1.2943267.
29. Zhai J, Xing Z, Dong S, Li J, Viehland D. Magnetoelectric laminate composites: an overview. J Am Ceram Soc. 2008;91(2):351–8. doi:10.1111/j.1551-2916.2008.02259.x.
30. Benveniste Y, Miloh T. Imperfect soft and stiff interfaces in two dimensional elasticity. Mech Mater. 2001;33(6):309–23. doi:10.1016/s0167-6636(01)00055-2.
31. Chen J, Guo J, Pan E. Wave propagation in magneto-electro-elastic multilayered plates with nonlocal effect. J Sound Vibrat. 2017;440:550–63. doi:10.1016/j.jsv.2017.04.001.

32. Zhu F, Wang B, Qian ZH. A numerical algorithm to solve multivariate transcendental equation sets in complex domain and its application in wave dispersion curve characterization. Acta Mech. 2019;230(4):1303–21. doi:10.1007/s00707-017-2025-y.
33. Ly D-K, Vu-Do H-C, Thongchom C, Nguyen-Thoi T. A multiscale and multiphysical numerical approach for sandwich multiphasehybrid fiber plates with smart composite facesheets. Eng Anal Bound Elem. 2025;173(03):106134. doi:10.1016/j.enganabound.2025.106134.